Schweizerische Eidgenossenschaft
Confédération suisse
Confederazione Svizzera
Confederaziun svizra

Department of the Environment, Transport, Energy and Communication DETEC
Swiss Federal Office of Energy SFOE
Energy Research

Final report

Characterization of high boiling point/synthetic fuels for HCCI and partially stratified Diesel engine combustion by means of optical experiments and global reaction models

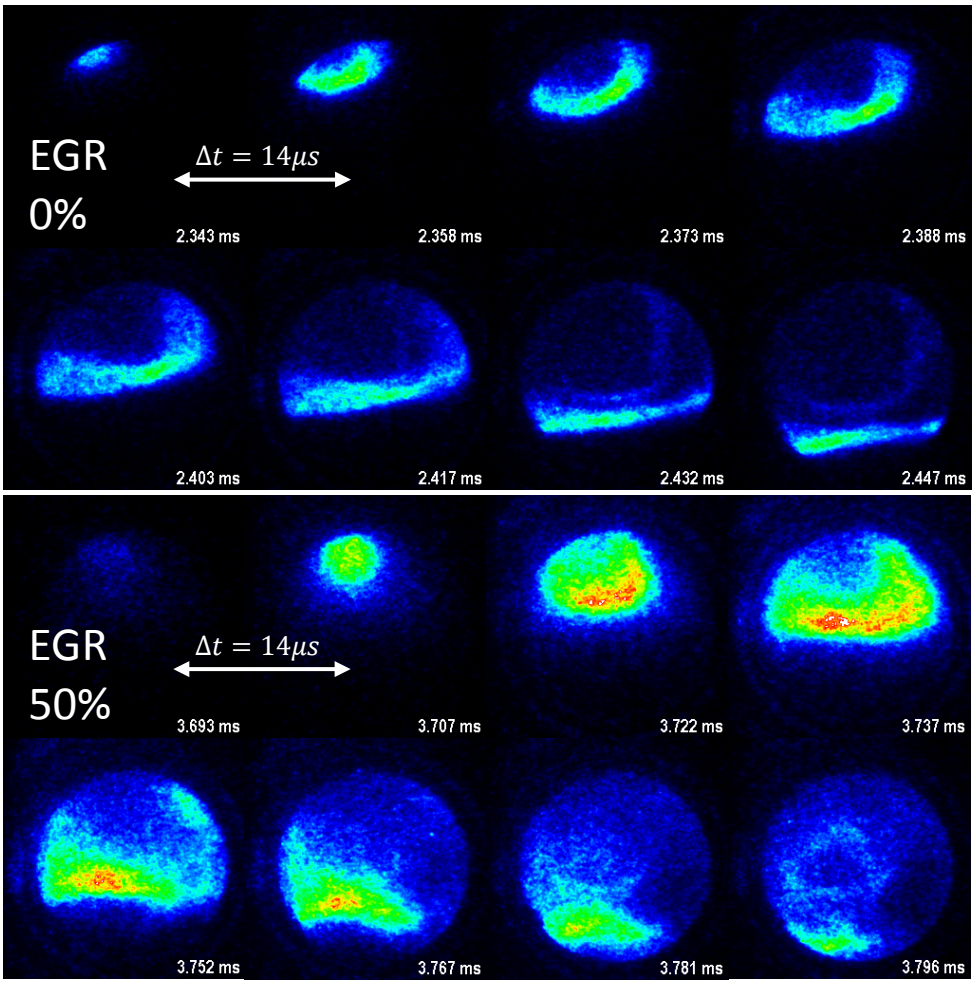

Characterization of high boiling point/synthetic fuels for HCCI and partially stratified Diesel engine combustion by means of optical experiments and global reaction models

Date: 3rd September 2016

Town: Zurich

Publisher:
Swiss Federal Office of Energy SFOE
Combution Research Programme
CH-3003 Bern
www.bfe.admin.ch

Co-financed by:
– Swiss Oil Association
Research Grant no. 3'34'12
– Research Association for Combustion Engines (FVV) eV
Project „Fuel Indices II./Kraftstoffkennzahlen II.“

Agent:
ETH Zürich
Institut für Energietechnik,
Laboratorium für Aerothermochemie und Verbrennungssysteme
Sonneggstrasse 3
CH-8092 Zürich
www.lav.ethz.ch

Authors:
Christopher Blomberg, blomberg@lav.mavt.ethz.ch
Dr. Dimitrios Mitakos, mitakos@lav.mavt.ethz.ch
Dr. Michele Bardi, bardi@lav.mavt.ethz.ch
Dr. Yuri M. Wright, wright@lav.mavt.ethz.ch
Dr. Bruno Schneider, schneider@lav.mavt.ethz.ch
Prof. Dr. Konstantinos Boulouchos, ETH Zürich, boulouchos@lav.mavt.ethz.ch

SFOE head of domain: Carina Alles, Carina.Alles@bfe.admin.ch
SFOE programme manager: Stephan Renz, renz.btr@swissonline.ch
SFOE contract number: SI/500801-01

The author of this report bears the entire responsibility for the content and for the conclusions drawn therefrom.

Zusammenfassung

In dieser Studie wurde die Zweckmässigkeit der Cetanzahl (CN) zur Charakterisierung der vollhomogenenen, kompressionsgezündeten Verbrennung (Homogeneous Charge Compression Ignition, HCCI) untersucht für verschiedene Kraftstoffe. Korrelationen zwischen CN und HCCI Selbstzündung wurden zuerst erarbeitet; im Anschluss daran wurden prädiktive Modelle entwickelt, die den komplexen Zündvorgang beschreiben. Hierzu wurden fundamentale experimentelle und numerische Untersuchungen von HCCI und teilhomomogenen (Partially-Premixed Compression Ingition, PCCI) Verbrennungsvorgängen durchgeführt. Surrogate mit gut definierten Eigenschaften und identischen CN der ursprünglichen Kraftstoffe wurden im optisch zugänglichen Einhubtriebwerk (RCEM) für weite motorische Bedingungen charakterisiert. Die bestimmenden Prozesse die zur Zündung führen sowie die relevanten HCCI-Kenngrössen wurden dabei identifiziert, namentlich Wärmefreisetzungen der Niedertemperaturzündung und der anschliessenden intermediate Phase, sowie Zündtemperatur. Zwei HCCI Modelle wurden erarbeitet und für die Surrogate weiterentwickelt: I) das 3-Arrhenius Modell zur Zündverzugsvorhersage, II) ein Modell für die Niedertemperaturwärmefreisetzung (Cool Flame model). Für die Parametrierung wurden neue Ansätze enwickelt welche Kalibrierung der Modellkonstanten für beliebige Kraftstoffe ermöglichen. Durch Kombination des 3-Arrhenius- und Cool Flame Modells mit einem Livengood-Wu-Zündintegral wurde ein prädiktives Modell zur Zündverzügsvorhersage im 0D und 3D-Kontext geschaffen; Validierung erfolgte anhand der RCEM-Daten, wobei ausgezeichnete Übereinstimmung mit den Messwerten der Surrogate demontriert wurde. Das 3D-Modell bildet darüberhinaus Einflüsse von Strömungsfeld, Stratifizierung (Mischung/Temperatur) und Wandwärmeverlusten ab. Dessen Vorhersagen in der RCEM zeigen im Vergleich zu einer 3D-CFD mit skeletaler Chemie gute Ergebnisse mit um Grössenordnungen reduzierter Rechenzeit. Eine erste Studie mit LES-CMC und RANS-CMC Verbrennungsmodellen von PCCI Verbrennung mit Mehrfacheinspritzungen (ECN „Spray A“) zeigte ebenfalls gute Übereinstimmung mit dem Experiment und ermöglichte ein vertieftes Verständnis der Wechselwirkungen der komplexen physikalischen Prozesse.

Résumé

Ce projet a étudié l’utilité de l’indice de cétane (CN) comme caractéristique de la combustion à allumage par compression à charge homogène (HCCI) pour différents carburants. Des corrélations entre l’indice de cétane et la tendance à l’auto-allumage ont été établies. Ensuite, de modèles prédictifs, capables de décrire le procès de l’allumage ont été développés. Une campagne d’investigations expérimentales et numériques de la combustion HCCI et partiellement homogène (Partially-Premixed Compression Ingition, PCCI) a fourni les données de base. A l’aide d’une machine à compression et expansion rapide (RCEM), un substitut aux propriétés bien-connues et à l’indice de cétane (CN) équivalent au combustible initial a été caractérisé sous des conditions semblables à celles dans un moteur à combustion. En particulier, le dégagement de chaleur pendant la phase d’allumage à température basse et la phase intermédiaire, ainsi que la température d’allumage ont été déterminés. Deux modèles prédictifs ont été développés pour les substituts : (1) le modèle « 3-Arrhenius » du retardement de l’allumage et (2) le modèle « Cool Flame » du dégagement de chaleur à température basse. Une nouvelle méthode de calibration des constantes de modélisation a été développée ; elle peut être appliquée à tout combustibles. La combinaison des modèles « 3-Arrhenius » et « Cool Flame » avec l’intégrale d’allumage Livengood-Wu fournit un modèle de prédiction du retardement de l’allumage dans un contexte 0D et 3D. Le modèle a été validé aux données RCEM et une coïncide excellemment avec les substituts. Le modèle 3D inclut l’influence du champ d’écoulement, de la stratification de mélange et de la température ainsi que de la perte de chaleur. Comparé à une simulation 3D-CFD, le temps nécessaire au calcul d’une prédiction fiable de la perte de chaleur pour l’RCEM est massivement réduit. Une étude préliminaire de la combustion PCCI à injection multiple (ECN « Spray A ») avec des modèles détaillés (LES-CMC et RANS-CMC) coïncide bien avec les données expérimentales et ouvre un aperçu approfondi de l’interaction complexe des processus physiques.

Summary

This research project investigates the appropriateness of the cetane number (CN) as an index for Homogeneous Charge Compression Ignition (HCCI) combustion for numerous automotive fuels. Correlations between CN and HCCI auto-ignition are presented, followed by development of predictive models which describe the complex auto-ignition process. To this end, HCCI and PCCI combustion processes were studied from a fundamental perspective both experimentally and numerically: surrogate fuels with identical CN as the original fuels were characterized in an optically accessible Rapid Compression-Expansion Machine (RCEM) over a wide range of HCCI relevant engine conditions to provide an experimental database for model validation. The driving factors leading to ignition, as well as the resulting parameters of interest for HCCI combustion were identified, namely low and intermediate heat release, and ignition temperature. Two HCCI models were developed and extended for the surrogate fuels: I) a 3-Arrhenius model, suitable for ignition delay prediction and II) a model for the low temperature heat release (Cool-Flame model). New methodologies for model parameterization are presented which allow for model constant calibration of virtually any fuel. By combining the 3-Arrhenius and Cool-Flame models with a Livengood-Wu ignition integral, a fully predictive methodology for low and high temperature ignition delays was established, which can be used in both 0D- and 3D-simulations. The parameterized 0D model is validated for the surrogate data from the RCEM showing excellent agreement. When used in a 3D context, effects of flow-field, wall heat loss and stratification (temperature and mixture) can be accounted for. Predictions in the RCEM compare well to calculations using 3D-CFD with semi-detailed kinetics, at computational costs lower by several orders of magnitude. Towards PCCI combustion, two detailed numerical approaches (RANS-CMC and LES-CMC) were applied to study highly transient multiple injection combustion (ECN “Spray A”) for one diesel-like and one low temperature condition. Ignition delays and flame structures are predicted well and the results provide valuable insights w.r.t. the complex physical processes.

Appendix

Final 3-Arrhenius parameters for all new fuels.

Fuel	n-Heptane	PRF41	TRF7.3	BVP9.1	BVP31.8	n-Decane
Low Temperature Parameters						
A_1	7.417E-10	7.341E-10	1.050E-10	2.788E-12	4.566E-11	6.023E-11
β_1	-1.033E-01	-2.269E-01	-1.230E-01	-2.188E-01	-2.246E-01	-2.205E-01
T_{A1}	1.107E+04	1.133E+04	1.252E+04	1.539E+04	1.369E+04	1.291E+04
b_1	0	0	0	0	0	0
c_1	0	0	0	0	0	0
d_1	0	0	0	0	0	0
e_1	0	0	0	0	0	0
Negative Temperature Coefficient Parameters						
A_2	2.669E-12	2.516E-11	7.510E-11	1.564E-11	6.872E-11	2.219E-20
β_2	-1.862E+00	-1.484E+00	-1.798E+00	-1.825E+00	-1.772E+00	-1.748E+00
T_{A2}	-2.279E+03	-1.011E+03	-2.967E+03	-2.542E+03	-1.072E+03	-1.725E+01
b_2	4.013E+00	3.459E+00	3.601E+00	3.812E+00	3.337E+00	6.278E+00
c_2	-1.159E+00	-1.696E+00	-1.230E+00	-1.253E+00	-1.336E+00	-1.298E+00
d_2	-2.024E-01	-1.899E+00	-2.090E-02	-1.826E-01	-6.296E-02	-2.791E-02
e_2	3.278E+02	6.223E+02	3.065E+02	3.418E+02	3.041E+02	3.194E+02
High Temperature Parameters						
A_3	1.697E-10	2.049E-09	2.100E-10	6.887E-11	4.758E-11	4.875E-13
β_3	-1.266E+00	-1.208E+00	-1.019E+00	-9.779E-01	-8.656E-01	-6.334E-01
T_{A3}	1.874E+04	1.543E+04	1.686E+04	1.796E+04	1.759E+04	2.185E+04
b_3	0	0	0	0	0	0
c_3	0	0	0	0	0	0
d_3	1.122E-01	5.927E-01	5.635E-01	4.767E-01	7.315E-01	3.224E-01
e_3	0	0	0	0	0	0
Statistics						
LT R^2 and RMSE	95.1% and 0.2ms	91.7% and 0.2ms	93.9% and 0.2ms	95.3% and 0.1ms	89.6% and 0.2ms	90.9% and 0.1ms
HT R^2 and RMSE	97.0% and 0.08ms	98.2% and 0.09ms	98.2% and 0.08ms	98.4% and 0.07ms	96.8% and 0.09ms	96.6% and 0.08ms

Final Cool-Flame model parameters for all new fuels

Fuel	n-heptane	PRF41	TRF7.3	BVP9.1	BVP31.8	n-decane
a	6.91	6.91	6.91	6.91	6.91	6.91
m	1.55	1.17	1.47	2.81	1.28	1.35
Δt_v						
b_0	0.64	0.73	0.63	0.39	0.33	0.10
b_1	0.20	0.26	0.22	0.19	0.23	0.25
b_2	-0.07	-0.08	-0.07	-0.05	-0.05	-0.10
b_3	0.23	0.32	0.26	0.32	0.25	0.42
R^2	93%	93%	93%	96%	79%	94%
RMSE	0.09	0.11	0.11	0.06	0.18	0.08
$Q_{LTR,tot}/Q_{tot}$						
$c_0 \times 10^{-2}$	5.70	8.04	7.84	14.70	16.02	1.75
$c_1 \times 10^{-2}$	-0.41	-1.01	-0.45	-0.72	-2.08	-0.10
$c_2 \times 10^{-2}$	0.29	0.27	0.17	0.03	0.16	0.88
$c_3 \times 10^{-2}$	2.39	1.01	1.78	-0.09	-0.15	2.39
R^2	97%	95%	93%	67%	91%	82%
RMSE $\times 10^{-2}$	0.45	0.64	0.61	1.07	1.46	0.92

Contents

List of abbreviations

Δ	Filter width
k	Turbulent Kinetic Energy
μ	Viscosity
τ_{ID}	Ignition delay
AHRR	Apparent Heat Release Rate
ASOI	After Start Of Injection
C_2H_2	Acetylene, soot precursor
CFD	Computational Fluid Dynamics
CH_2O	Formaldehyde, low-temperature combustion indicator
CMC	Conditional Moment Closure
CPU	Central Processing Unit
ECN	Engine Combustion Network
LES	Large Eddy Simulation
LTC	Low Temperature Combustion
MF	Mixture Fraction
MFT	Total Mixture Fraction
NVH	Noise Vibration Harshness
OC	Operating Condition
OH	Hydroxide, high temperature combustion indicator
PAH	Polycyclic Aromatic Hydrocarbons
PDF	Probability Density Function
PLIF	Planar Laser Induced Fluorescence
RANS	Reynolds Averaged Navier-Stokes
RIF	Representative Interactive Flamelet
SGS	Sub-grid Scale
SOI	Start of Injection
TPDF	Transported Probability Density Function

Executive summary

Homogeneous Charge Compression Ignition (HCCI) combustion seeks to combine the emission advantages of lean or dilute premixed combustion with the efficiency of the compression ignition process. The lack of an actuator (spark or injection event) however leads to a predominantly kinetically controlled start of combustion, strongly dependent on the fuel's ignition propensity. Understanding the specific ignition behaviour of a fuel undergoing HCCI combustion is hence paramount and this project seeks to elucidate if the cetane number – a property widely in use for compression ignition of fuels – is applicable also for HCCI. To this end blends of different automotive fuels, including oxygenated compounds have been studied in full metal engines (at IVK/University of Stuttgart) and corresponding surrogates were characterized in a Rapid Compression Expansion Machine (RCEM, at LAV/ETH Zurich). High-speed optical data in combination with thermodynamic analysis from the latter test rig provided key insights with respect to the low temperature ignition process, the heat release during the low- and intermediate phases leading to high temperature combustion. The key findings reported using well-defined surrogates in the fundamental test rig are fully supported by measurements on the full metal engine running on the corresponding automotive fuels.

With this knowledge, predictive HCCI engine models for potential engine applications were developed, which include I) a modified 3-Arrhenius auto-ignition model, II) an improved low temperature heat release rate model and III) a model for the prediction of high temperature heat release by combining the former with an ignition integral of the Livengood-Wu type. The latter can be used both in a 0D-context for rapid prediction of low- and high-temperature ignition delays for changes in thermodynamic conditions and charge composition (fuel type, equivalence ratio, EGR). When used in a 3D-CFD context, effects of thermal and composition stratification can be accounted for allowing changes is engine design to be investigated at computational cost which are lower by several orders of magnitude compared to 3D-CFD using semi-detailed kinetics.

Towards PCCI combustion, 3D-CFD using RANS and LES turbulence models together with a state-of-the-art Conditional Moment Closure (CMC) combustion model were successfully applied to study split-injection events, resembling contemporary PCCI injection schedules. Experimental data from the Sandia National Laboratories constant volume combustion chamber at Diesel-like ambient conditions (60 bar, 900 K) and for low temperature combustion (50 bar, 750 K) was used for validation (ECN "Spray A"). *n*-dodecane fuel follows a schedule of 0.5 ms injection – 0.5 ms dwell – 0.5 ms injection. Ignition delays and general flame structures of both the operating conditions are predicted well by RANS-CMC and LES-CMC and both numerical approaches show considerable promise to model highly transient split-injection combustion. It is important to note that this study was undertaken in view of transitioning towards more complicated injection strategies of PCCI leading to partially premixed combustion and thereby "bridging the gap" between pure HCCI models and well-established diffusion combustion models at LAV/ETH Zurich.

1 Introduction

Increasingly stringent emission regulations and the high variability of oil prices are forcing engine manufacturers to re-think their engine development programs. Overcoming the trade-off between emission reduction and efficiency optimization is a central theme. HCCI combustion and PCCI are known to potentially achieve diesel like efficiencies, while drastically reducing soot and engine-out nitrogen oxide (NOx) emissions. This low emission window is shown in Figure 1.

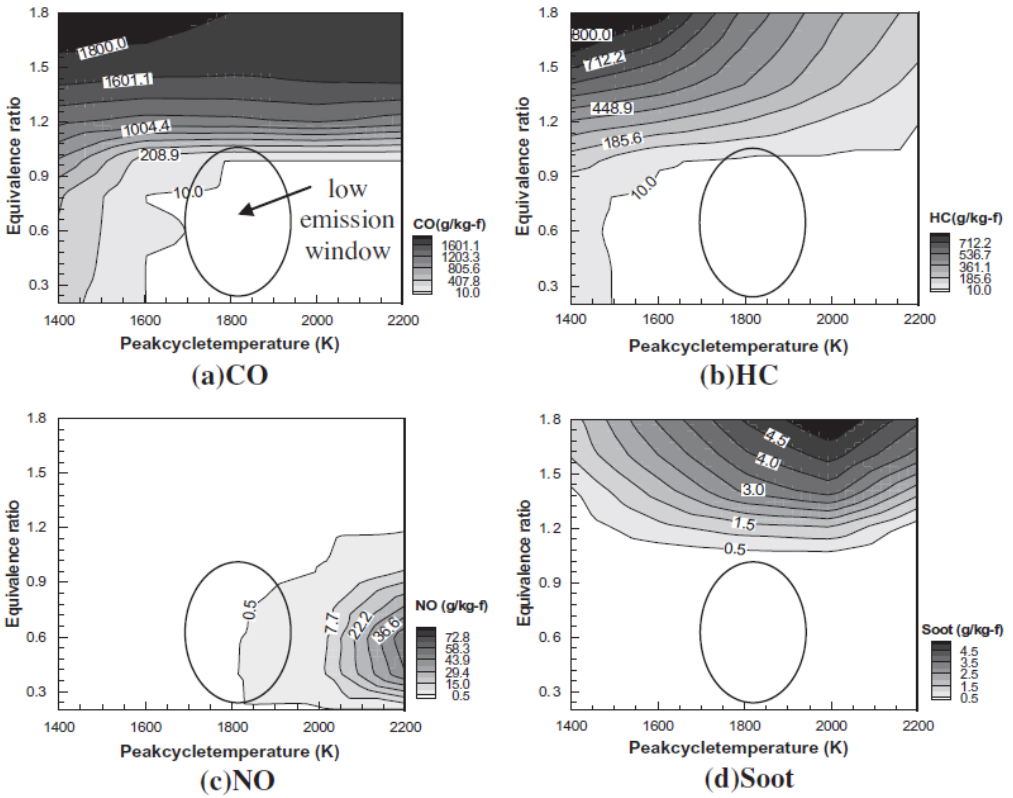

Figure 1 - Predicted HCCI engine out emissions for (a) CO, (b) HC, (c) NO and (d) soot on equivalence ratio vs. peak cylinder temperature plots [1].

In an HCCI combustion process, the fuel is typically introduced very early into the combustion chamber to support homogenization. This eliminates the possibility to control the start of combustion by an external source, e.g. fuel injection or spark-plug. Instead, the start of combustion is determined by the charge state (pressure, temperature, residual gas), the mixture formation and in particular by the auto-ignition characteristics of the fuel. A particular characteristic of a HCCI fuel is that it exhibits either a single or two-stage auto-ignition [2]. This phenomenon is fuel- and operating condition-specific, and is illustrated for two example fuels (PRF80 and iso-octane) in the heat release rate (HRR) plot in Figure 2.

The build-up of heat – caused by chain branching exothermic reactions – until the main ignition event is of vital importance for auto-ignition. Therefore the question for auto-ignition is, given an operating condition and fuel, how fast does the charge reach the necessary heat for main ignition.

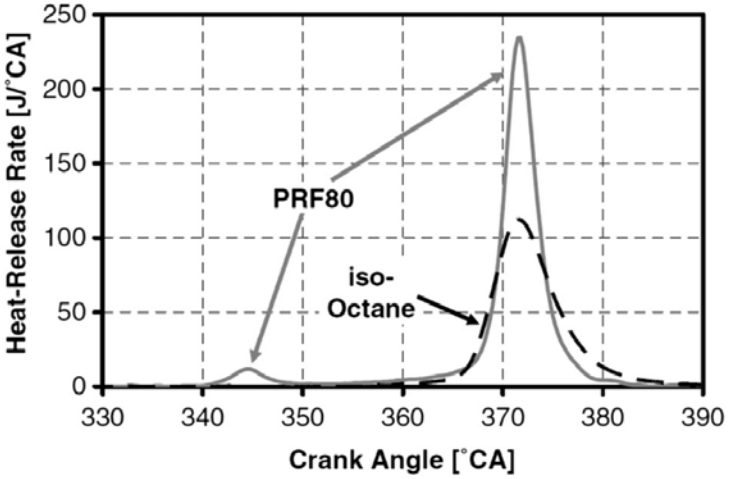

Figure 2 - Heat release rate (HRR) of HCCI combustion in an engine running on PRF80 or iso-octane [3].

To answer this question a more detailed overview of fuel auto-ignition properties is necessary, which could go far beyond the conventional description of ignition performance by cetane number (CN). Consequently, there is a particular need to describe ignition delay depending on the charge states, and the fuel properties under homogeneous, auto-ignition conditions. The definition of a new fuel index and a methodology to determine it needs to be investigated. The outcome can then be developed into predictive models which depend on operating conditions at the start of combustion. These tools can then be directly applied to the development of HCCI engines.

PCCI combustion makes use of partial mixture stratification to have more control of the onset of ignition [4]. This can be accomplished by e.g. multiple direct injections into the combustion chamber. The onset of ignition is more closely coupled to spray mixing than HCCI, however chemical kinetics of the fuel still play an important role. Therefore, understanding the interaction between multiple injections and their influence on ignition, emission formation/distruction and combustion phasing is essential to further progress PCCI technology.

1.1 Starting Point and State of the Art

The FVV predecessor Fuel Indices I project has shown that it is possible to produce a good agreement between measured shock-tube ignition delays and engine (run in HCCI mode via an Atomizer) measured ignition delays [5–9]. This transferability of results from the perfectly mixed shock tube shows that a motor can reach maximum homogeneity with a customized external mixture formation. This can serve as a reference for a maximum of homogeneous diesel combustion (HCCI). This transferability could be detected by means of a so-called 3-Arrhenius approach [10][11], which had been calibrated for each fuel on the basis of shock-tube measurements and applied to the motor by means of the ignition integral method of Livengood and Wu [12]. Unfortunately it was not possible to measure the heavy diesel fuels in the shock tube [5].

For this reason, one aim of this project was to have engine-like measurements provide the necessary calibration data for HCCI modeling. In total three HCCI models were developed. The model presented in [8] was developed by IVK Stuttgart while the models found in [13,14] by LAV Zurich. [8] and [13,14] are Arrhenius-like auto-ignition models, which necessitate experimental data to predict ignition delays. Thus, they are not stand-alone models. The third model [13] addresses this point and provides a fully predictive auto-ignition model.

To increase the understanding of interactions between short pilot injections and their effects on combustion, the recent experimental work of Skeen et al. [15,16] was taken as a reference point for model validation and development. Here split-injections using the “Spray A” injector in a constant volume

chamber with high optical accessibility and *n*-dodecane (a common diesel fuel surrogate for which detailed chemical kinetics are available, e.g. [17]) as a fuel were undertaken for a high temperature diesel-like ambient condition and a low temperature ambient condition. The goal was to validate current models available at LAV for the simpler split-injection setup, with the prospect of moving towards full engine simulations running at PCCI conditions. Therefore, LAV computed detailed 3D-CFD simulations where both RANS and LES flow field solvers coupled with the CMC combustion model were investigated.

Another goal of this project was to develop a new fuel indexing methodology for homogeneous and partly homogeneous compression ignition combustion. This was done by IVK and is presented in their corresponding part of the final report.

2 Measurements in the Rapid Compression Expansion Machine (RCEM)

In this section, the RCEM experimental apparatus is presented and the design modifications carried out in this project are summarized. Subsequently, the employed measurement techniques are discussed; next the fuels tested and operating conditions are detailed. Finally, the main outcomes of the measurement campaign are presented.

2.1 Improvements and modifications of the RCEM

2.1.1 Intake / exhaust valves

In the original design of the rapid compression expansion machine (RCEM) the valves controlling the intake and exhaust pipes of the cylinder where placed a few hundred millimetres away from the cylinder head, thereby creating relatively big “dead” volumes. Such large crevice volumes make it very challenging to determine heat release rates for combustion processes accurately since the exact amount of air (or air-fuel mixtures) trapped in these pipes is difficult to estimate.

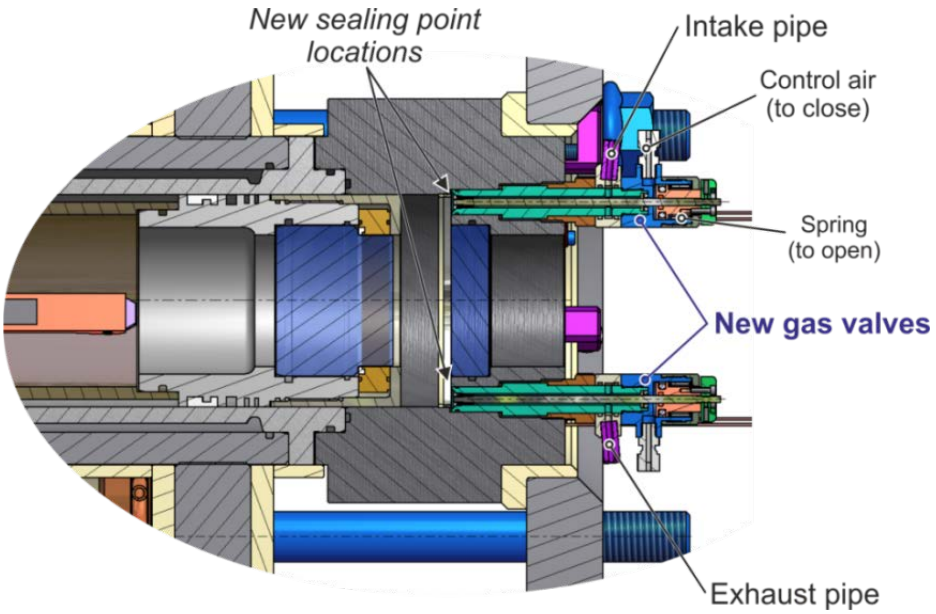

Figure 3 - Vertical cross section through the cylinder head and the new gas valves of the RCEM.

The solution to address these difficulties consists of new miniaturized gas valves placed directly inside the cylinder head (cf. cross section in Figure 3). This moves the sealing point of the intake and exhaust pipes to the cylinder head (as in a real engine), thereby completely eliminating the dead volumes of the pipes.

2.1.2 Additional window in the cylinder head

The new cylinder head for the RCEM (as shown in Figure 3 and Figure 4) is also equipped with a window which allows for an optically free diameter of Ø52 mm (i.e. 62% of the cylinder diameter) through both the piston and the cylinder head. This arrangement permits the use of backlit optical measurement techniques such as shadow imaging or Schlieren which is very advantageous for experimental investigations in the context of liquid fuel injection.

Due to the new window the position of the injector(s) had to be moved away from the cylinder axis: In case of the hollow cone injector that is used for mixture preparation before the start of compression this has no negative effect since there is plenty of time for evaporation and mixing before the compression stroke starts (gaseous fuels or liquid fuels with evaporation temperature below the controlled cylinder wall temperature). In case of the Common Rail injector, a multi-stream injector with a large umbrella angle is employed, where all nozzle holes except for one are closed. The lateral placement further enables roughly twice the penetration length to be observed through the windows compared to the case of a centrally located injector, i.e. the spray is visible from about 10 mm to 60 mm distance from the nozzle, i.e. a spray length representative of engines with piston bowl diameters in the order of 120 mm (cylinder diameter 160 mm).

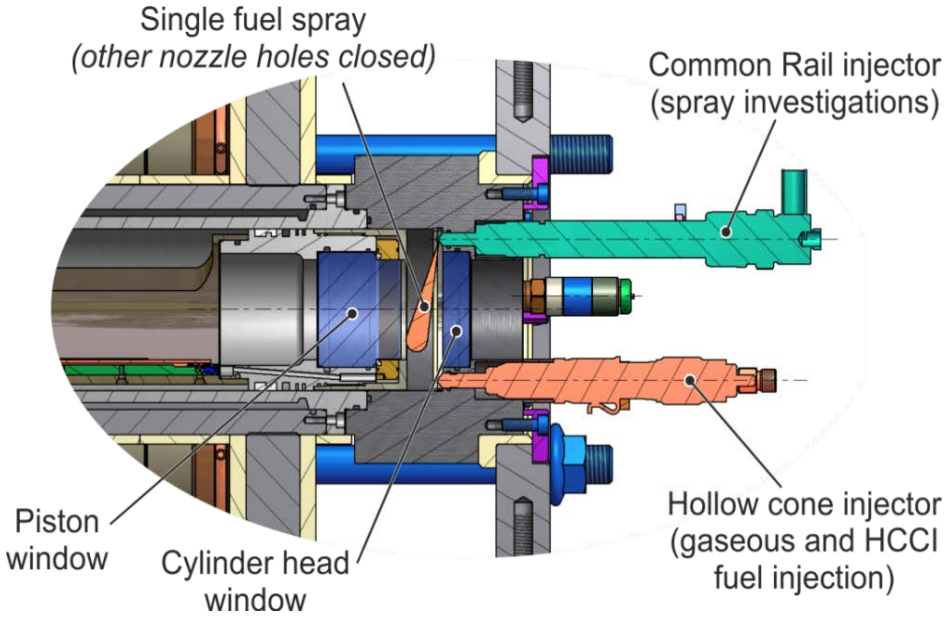

Figure 4 - Horizontal cross section through the new cylinder head of the RCEM with the new axial window and the two fuel injectors.

Figure 5 shows the new cylinder head as it is installed in the RCEM. Various elements of the optical setup can be seen through the head window, namely the piston, piston window and the 45° mirror in the piston rod as well (the red glow visible in the window stems from the high power LASER diode used as the light source).

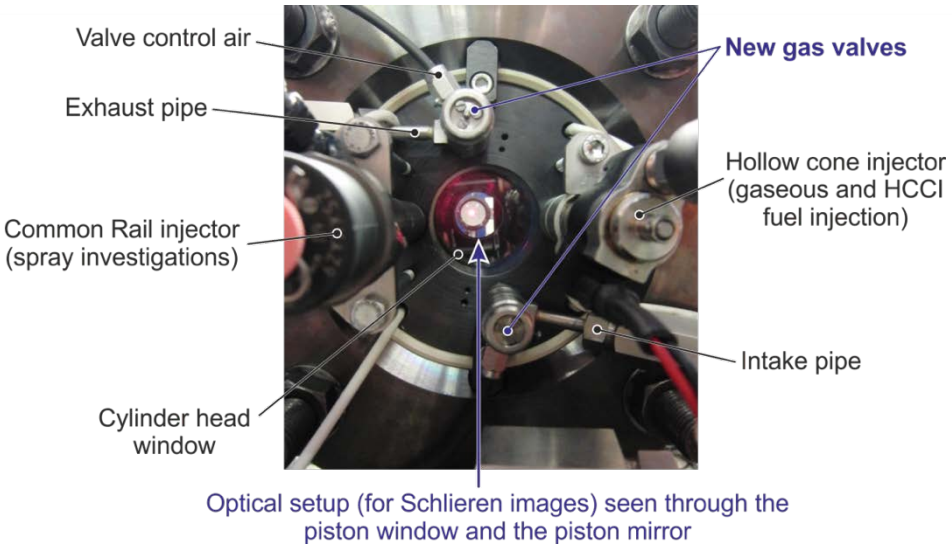

Figure 5 - The new cylinder head with the window, the gas valves and the two injectors.

2.1.3 Low range absolute pressure sensor

Precise measurement of the loading pressure is fundamental for the accuracy of the measurement. However, due to the high pressures reached during the combustion a low pressure sensor must be placed outside the test chamber and the measurement can only be performed before the intake valve closes, while the in-cylinder pressure is recorded with a high range sensor (0-20 MPa).

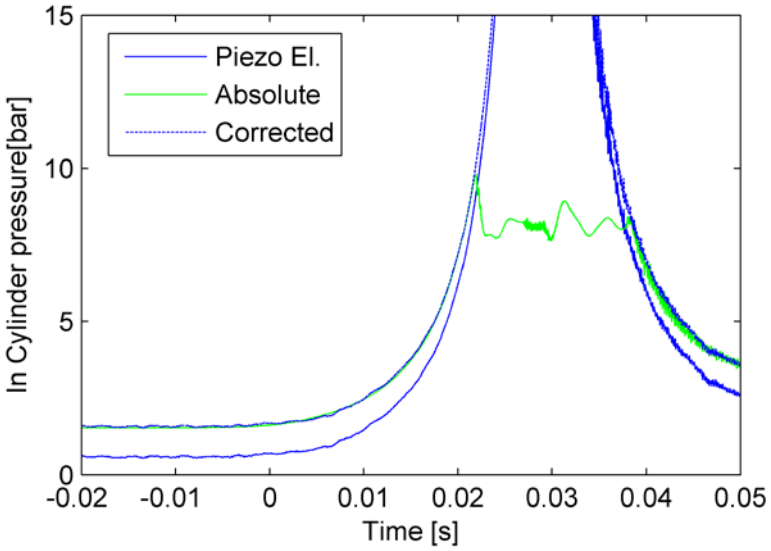

Figure 6 – Exemplary measurement of the low-range absolute pressure (green) and the hereby corrected relative high pressure measurement. The low range pressure sensor is isolated as soon as the cylinder pressure reaches 10bar.

To solve this problem, a low range piezo-resistive pressure sensor (0-1 MPa) was coupled to a pressure switch: the device was mounted so that the sensor can measure the pressure directly within the cylinder until its maximally measureable pressure is reached; at this point the switch closes and isolates the sensor from the high pressure reached in the cylinder that would destroy the sensor. In this way, a more

correct estimation of the loading pressure (i.e. cylinder charge mass) can be performed and the pressure measured by the piezo-electric sensor (relative) can be pegged more accurately (see Figure 6).

2.2 Measurement techniques

Apart from the thermodynamic analysis based on the cylinder pressure an piston position measurement a number of optical measurement techniques have been applied:

2.2.1 High speed OH* chemiluminescence imaging

A high speed camera (LaVision HSS6) combined with a fast intensifier (LaVision IRO) was used to detect the region where HTR takes place by filtering the light emitted from the combustion with a 310±5 nm filter. The high frame rate of the camera (68 kHz) and the short shutter time (0.5 to 10 µs) allows to resolve the short time scales in which the HCCI ignition and combustion takes place.

2.2.2 LTR chemiluminescence detection

The LTRs are characterized by very weak emissions from aldehydes between 350 and 500 nm. Even though the light emission is very weak, the heat release during this phase is crucial for the phasing of the HCCI combustion. Since this are the first reactions of the combustion process no light from possible broadband soot emissions later on can falsify the signal at this time. A photomultiplier was used to record the light emitted by the LTR combustion through filtering at a wavelength of 425±25 nm. The gain of the sensor was fixed close to the maximum level to ensure highest sensitivity to characterize the LTR, leading however to saturation during the later stages.

2.2.3 High-speed spectroscopy

A spectrograph coupled with an intensified high speed system recorded the spectrum (from 230 to 780 nm) emitted by the combustion at high-speed (50 kHz) and relatively short gating time (0.5 – 18 µs). The obtained results allow to better identify the different phases of the combustion and provide a deeper understanding of the signal captured by the other optical devices.

2.3 Fuels and operating conditions

A set of surrogate fuels were chosen in order to reproduce the main features of commercial fuels currently available on the market for which further details can be found in Table 1. The exact composition of the surrogate fuels was measured by Intertek Group plc to ensure the cetane number of the original fuels. To this end, high precision derived cetane number (DCN) measurements were carried out in a constant volume combustion chamber (CVCC) according to a new ASTM method D7668. Both original and surrogate fuels are shown in Table 1.

	Original Fuels			Surrogate Fuels		
	Low CN (≈38)	**Mid CN (≈50-55)**	**High CN (≈70)**	**Low CN (≈38)**	**Mid CN (≈50-55)**	**High CN (≈70)**
Non-Oxygenated	CN 39.6 57.5%$_{Vol}$ DK B0 + 42.5%$_{Vol}$ Eurosuper	CN 55.6 DK B0-1	CN>74.6 HVO	**PRF41** (CN 39.6) 41%$_{Vol}$ iso-Octane + 59%$_{Vol}$ n-Heptane)	**n-Heptane** (CN 55.28)	**n-Decane** (CN 76)
	-	CN 55.8 DK B0-2 + EHN	-	-	**TRF 7.3** (CN 51.42) 92.7%$_{Vol}$ n-Heptane + 7.3%$_{Vol}$ Toluene	-
Oxygenated	CN 36.5 66.5%$_{Vol}$ DK B0 + 33.5%$_{Vol}$ ETBE (4.4%$_{Mass}$ O_2 content)	CN 55.2 64%$_{Vol}$ DK B0 + 36%$_{Vol}$ RME (4.2%$_{Mass}$ O_2 content)	-	**BVP 31.8** (CN 37.8) 68.2%$_{Vol}$ n-Heptane + 31.8%$_{Vol}$ n-Butanol (7.67%$_{Mass}$ O_2 content)	**BVP 9.1** (CN 50.05) 90.9%$_{Vol}$ n-Heptane + 9.1%$_{Vol}$ n-Butanol (2.29%$_{Mass}$ O_2 content)	-

Table 1 – Original (left) and the corresponding surrogate fuels (right).

HCCI combustion of all the fuels shown above have been studied at different operating conditions. The special in-house designed cylinder liner and cylinder head enable a fine control of the wall temperature in the different areas of the chamber, and therefore homogeneous loading temperatures can be obtained. The test matrix was built by varying the following boundary conditions, resulting in a total 18 operating conditions.

– Loading temperature (T_w): 110 – 135 – 160 °C

– EGR percentage: 0 – 25 – 50%

– Load level (λ): “high” and “low” (constant mass of fuel)

For *n*-decane, only two variations in the test matrix were possible, namely in EGR and loading pressure, due to the relatively high boiling point of this fuel necessitating the temperature settings of the liner/head heating system at the maximum value of 185 °C.

At the different values of EGR, the fuel mass injected into the cylinder before compression was kept constant, the resulting lambda values are presented in Table 2.

Load	**low**	**high**
EGR [%]	λ	
0	3.5	2.5
25	2.625	1.875
50	1.75	1.25

Table 2 – Load level, EGR rate and the corresponding air-fuel equivalence ratio.

When the test matrix was applied to the different fuels the air-fuel equivalence ratio was kept as in the table. Taking into account the different lower heating values of the fuels, the energy injected in the system therefore slightly differs from one case to the other; Figure 7 presents the chemical energy “injected” in the different cases.

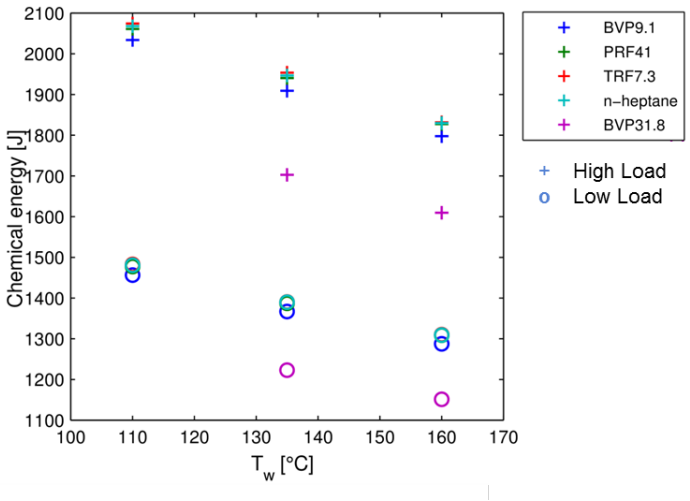

Figure 7 – Effective chemical energy "injected" for all fuels and load cases.

2.4 Experimental results

The measurements performed within this project resulted in two major achievements:

– Provide ignition delay and low temperature release rate data for the modeling validation

– Gain more understanding on the HCCI combustion process from the optical diagnostics

Since the first point will be presented in detail in the modeling validation section of this report (work package 2a), this part will present the results concerning the second point.

2.4.1 Oxygenated fuels show lower LTR heat release when compared to non-oxygenated fuels of similar cetane numbers

The plots in Figure 8 show one of the important findings of the experimental campaign: as expected, when moving from a high Cetane number fuel, i.e. *n*-heptane, to a lower cetane number fuel, e.g. PRF43 or BVP31.8, the integral low temperature heat release Q_{LTR} decreases significantly. However, when comparing two fuels of similar cetane number but with different oxygen contents (PRF41 and BVP31.8), it can be seen clearly that the oxygenated fuel has an inhibiting effect on the LTR. On the same plot it is also interesting to observe that EGR and loading temperature also exhibit a significant impact on Q_{LTR}: increasing the temperature or the EGR level causes a decrease in the integral LTR.

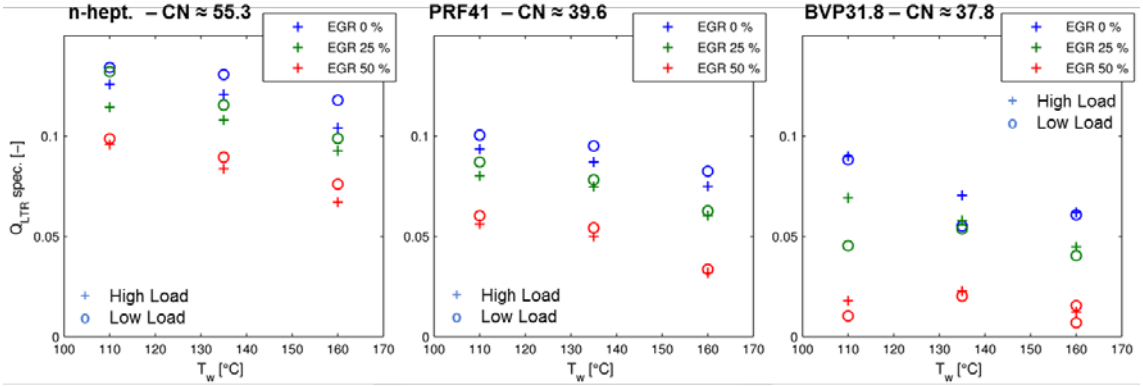

Figure 8 – Integral low temperature heat release (Q_{LTR}) measured for different fuels. *n*-heptane and two lower cetane number fuels: the different oxygen content of PRF41 and BVP31.8 is reflected in different Q_{LTR}.

Important results have further been achieved by the application of the LTR chemiluminescence measurement: the plots in Figure 9 show the heat release rate calculated from the thermodynamic analysis together with the LTR chemiluminescence signal for one single stroke. The comparison between the two signals suggests that:

– the LTR chemiluminescence photomultiplier is sensitive enough to detect the light emission during this phase of the combustion;

– the timing corresponding to the local maximum in the heat release corresponds to the local maximum observed in the LTR signal. This fact underlines a good potential of the technique to detect the timing of the LTR and that

– the shape of the curve is very similar, suggesting that the LTR signal can serve as a measure of the intensity of the heat release during this phase.

In order to validate the technique this comparison has been generalized in Figure 10 on the left hand side, the timing of the local maximum is compared for all the conditions at which this technique was applied (different fuel, different loading temperatures and different EGR levels). The plot shows a remarkable correlation between the two measurement techniques.

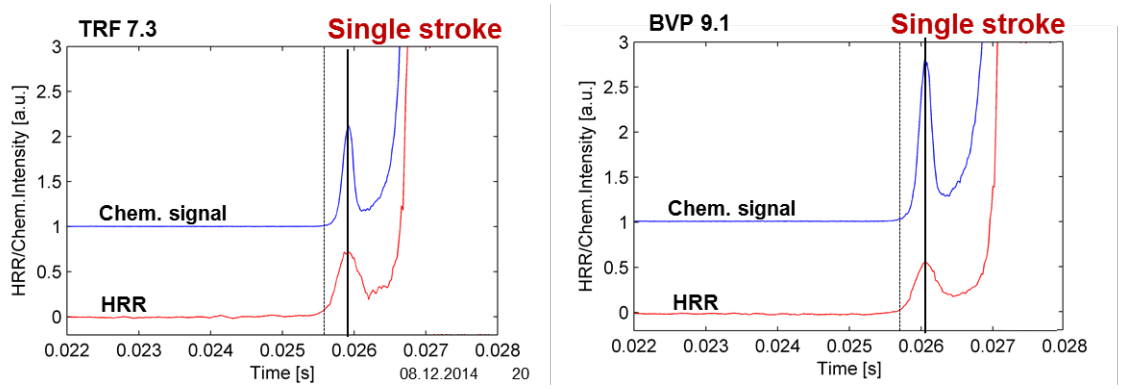

Figure 9 – Heat-release rate calculated by the pressure signal and chemiluminescence signal recorded by the LTR photomultiplier for two different fuels. The black vertical lines underline the good correlation between the signals.

On the right hand side of Figure 10 the same comparison is done for the magnitude of the heat release and chemiluminescence intensity peak. Even though the measurements refers to two different

magnitudes (Watt in one case and voltage in the other) a certain relationship can be observed between the two measurement and it can be concluded that the intensity of the LTR chemiluminescence signal can give a qualitative estimation of the heat release rate during this period as well.

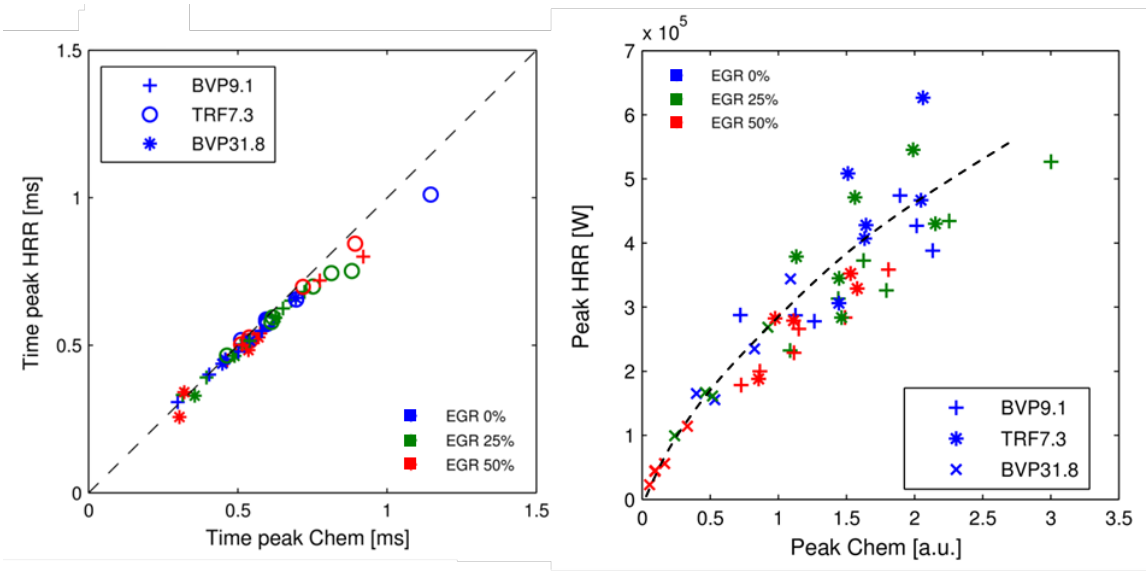

Figure 10 – Global comparison of chemiluminescence and HRR. The timing of the relative maximum (left hand side) and the magnitude of the relative maximums is shown for all the cases.

2.4.2 Heat release rate, HTR (OH*) and LTR (Aldehydes) chemiluminescence and spectroscopy

Results obtained by the different techniques applied are presented together, highlighting the features of the different phases of the combustion for a sample test condition. The compiled graph is composed of different plots as follows. Left column: heat release rate compared to the evolutions of LTR, OH* chemiluminescence and wavelength vs. time plots of the light spectrum (color represents intensity). The right hand side shows the spatial distribution of OH* chemiluminescence (upper) as seen through the window and the light spectrum (lower) at the time instant (t=2.014 ms before TDC) which is indicated on the left plots by the vertical bar.

2.4.2.1 LTR phase

As can be seen in Figure 11 neither the spectroscope nor the OH* camera detects any signal during the LTR phase. This is due to the very low intensity of the emitted light. Increasing the gain of the image intensifiers could enable a detection of these emissions, but could result in a destruction of the intensifiers during later, much brighter phases of the combustion.

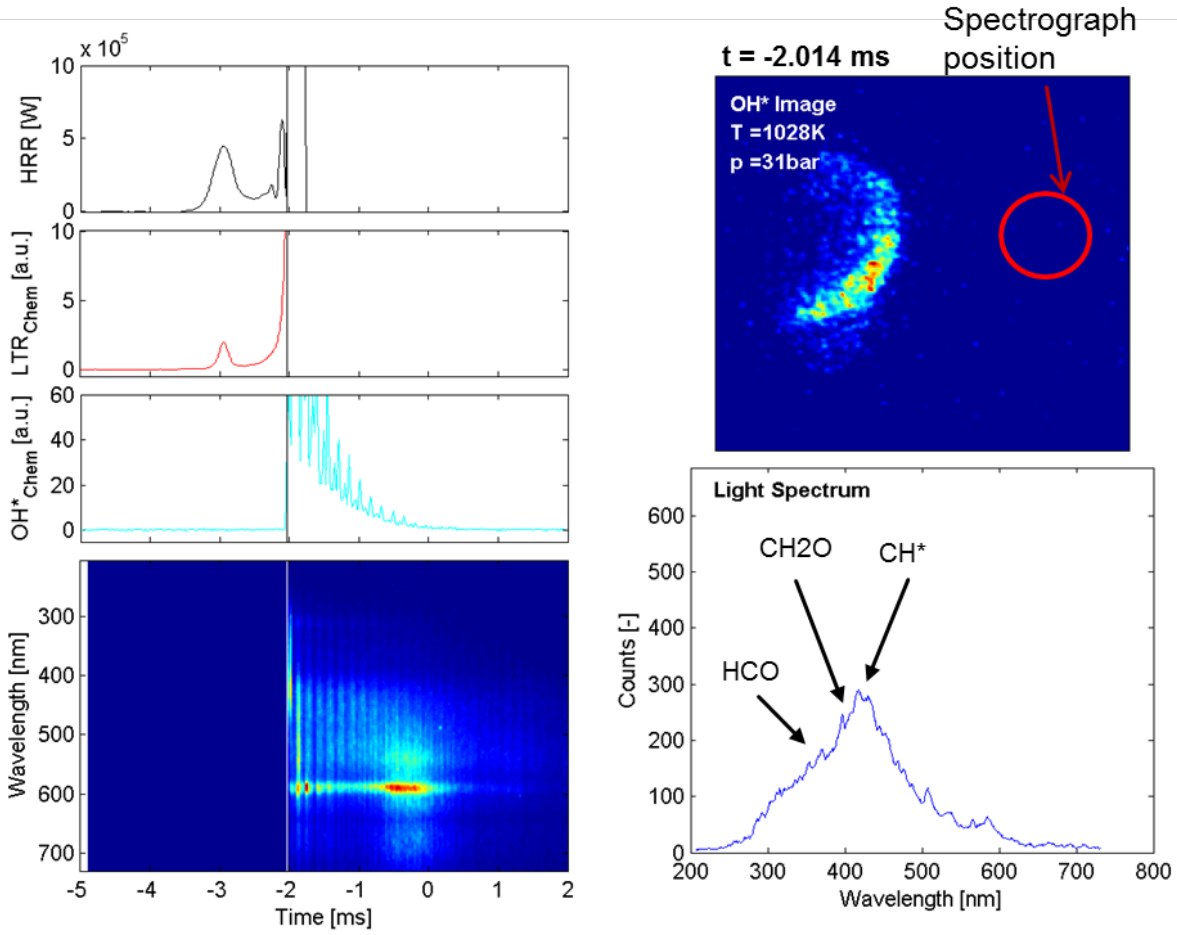

Figure 11 – Comparison of HRR, LTR and OH* chemiluminescence evolutions (left), spatial distribution of OH* (upper right) and light spectrum (lower right) for the time instant of 2.014 ms before TDC. The timing of the relative maximum (left hand side) and the height of this relative maximum is shown for all cases.

2.4.2.2 HTR phase

The beginning of the HTR is characterized by a strong rise of the HRR, a corresponding steep increase (and saturation) of the LTR chemiluminescence detection signal as well as the first observation of the OH* signal. Even though this combustion mode is supposed to be homogeneous, the spatial distribution of the OH* chemiluminescence signal in the images show a propagating front which bears some resemblance to flame propagation in spark ignited engines. However, two main differences clearly distinguish this combustion mode from a turbulent premixed flame:

– The speed at which this front is travelling (~500 m/s) is well above any laminar/turbulent flame speed.

– Chemiluminescence emissions are present on both sides of the front indicating that the chemical reactions are already taking place in all the combustion chamber and not only behind this front.

These phenomena can be explained by the compression wave that is generated from the first heat release taking place in the chamber. Even though the mixing of the fuel is homogeneous the in-cylinder turbulent flow field can be expected to lead to significant stratification in temperature during the compression [18] and therefore cause some spots to ignite slightly before others. The heat release caused by this ignition creates a local increase in the pressure that propagates as an acoustic wave. Since all the remaining fuel in the chamber is very close to the point of self-ignition, the small increase in pressure stemming from the acoustic wave is enough to start the self-ignition of the fuel. This

phenomenon can also be viewed as a sequential ignition. It is also important to remark that the duration of this event is very short, it generally takes less than 100 µs for the front to travel through the entire observable domain.

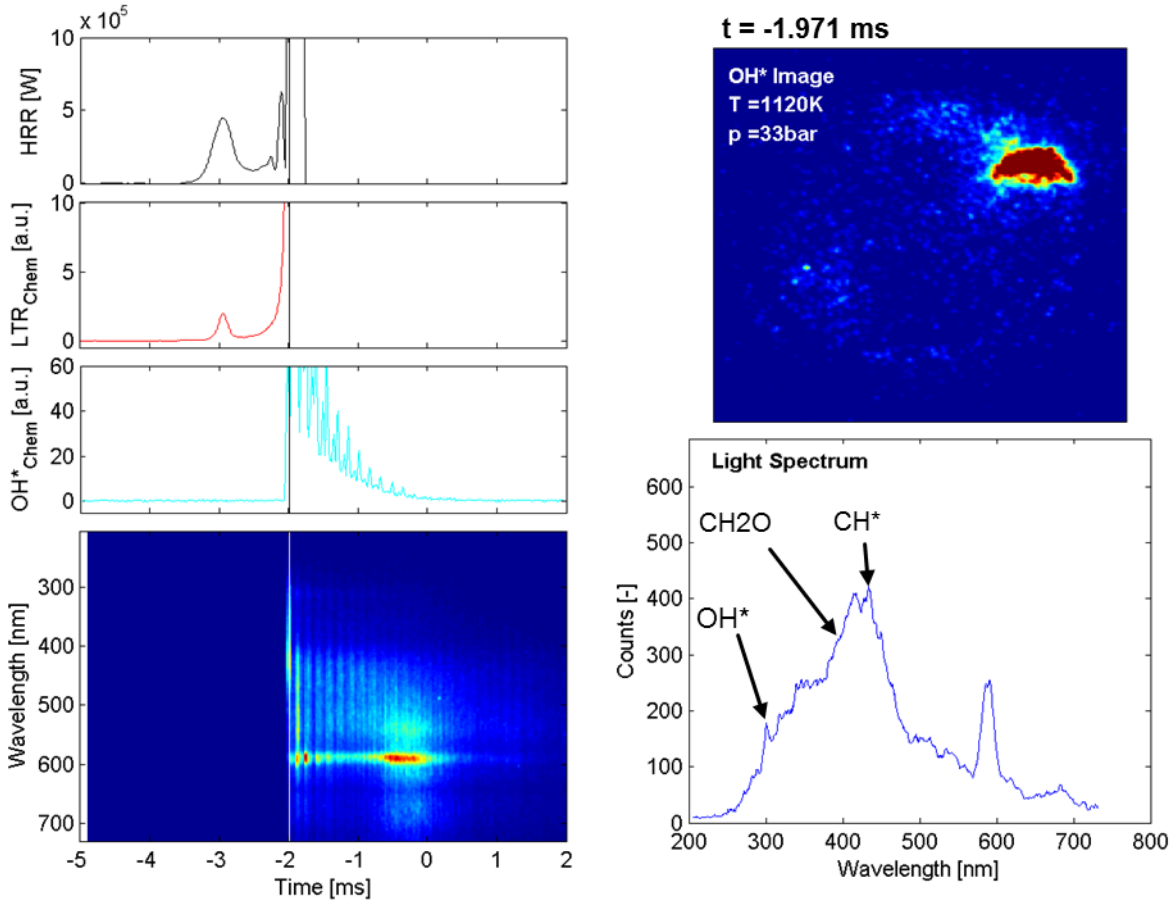

Figure 12 – Comparison of HRR, LTR and OH* chemiluminescence evolutions (left), spatial distribution of OH* (upper right) and light spectrum (lower right) for the time instant of 1.971 ms before TDC. The timing of the relative maximum (left hand side) and the height of this relative maximum is shown for all cases.

The entire amount of fuel reacts in a very short time (about 200 µs). However, some heat release is still taking place afterwards, which is proved by the slight peak at 308 nm (OH) observed with the spectroscope. It is believed that this phase of the combustion is related to the colder boundary layers close to the walls and crevices. However, it has to be underlined that the amount of heat released during this period is negligible compared to the total amount.

2.4.2.3 After-burn processes

As shown in Figure 13 even after a relatively long time from the beginning of the combustion significant emissions can still be recorded: to this purpose the interpretation is not univocal, but an important aspect has to be underlined: the top dead center is reached by the piston after the combustion, and therefore, even though no chemical reactions are taking place anymore, the temperature is still increasing leading some molecules to exited states. Moreover, the recorded emissions show a maximum slightly before top dead center, in agreement with the hypothesis of a relationship between emissions and temperature. Looking through the literature it can be observed that the spectrum observed can be related to exited states of CO_2 and O_2.

Finally, a prominent peak is observed at 590 nm: this unexpected peak is observed with different fuels and at almost all conditions tested. The peak matches the Na line pretty well, and even though sodium is not expected to be in the fuels a small quantity is present in the combustion chamber because it is contained in the grease used for the lubrication of the piston/cylinder.

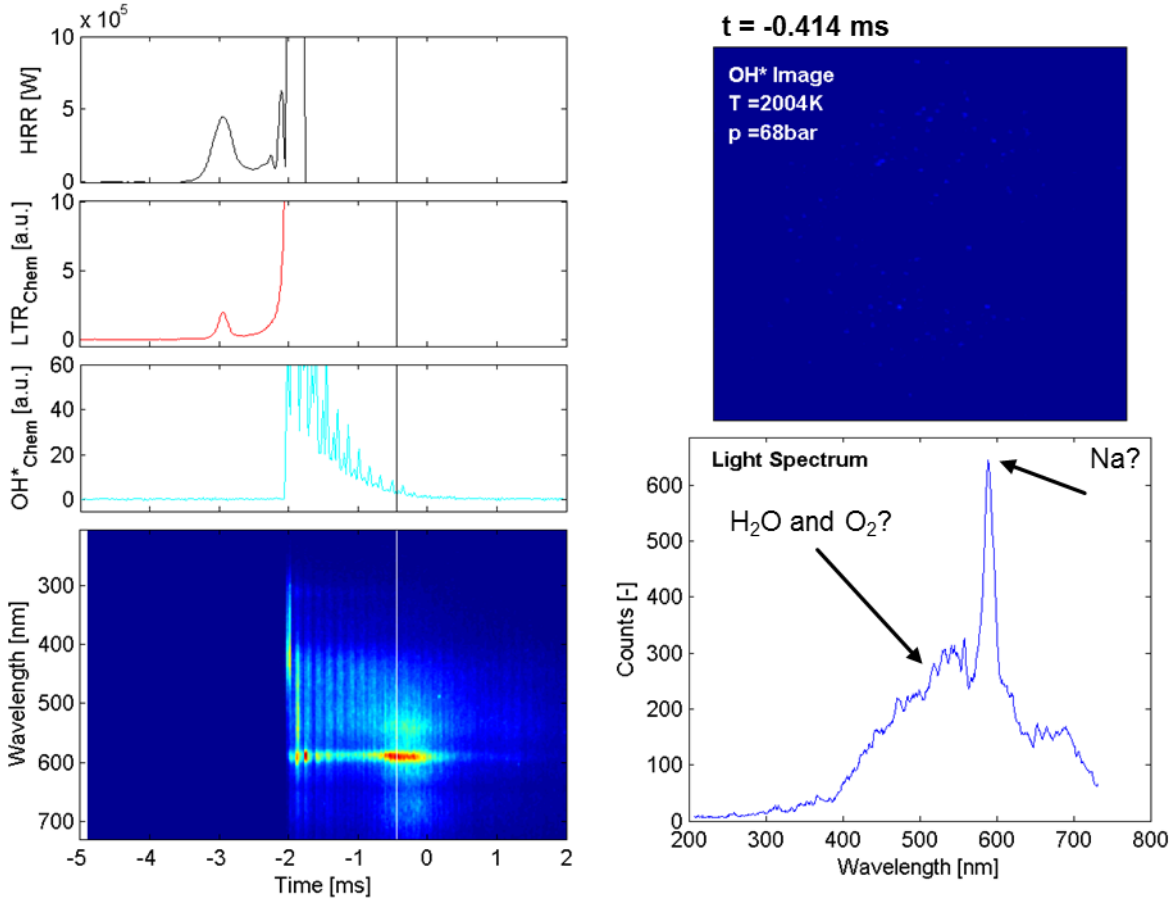

Figure 13 – Comparison of HRR, LTR and OH* chemiluminescence evolutions (left), spatial distribution of OH* (upper right) and light spectrum (lower right) for the time instant of 0.414 ms before TDC. The timing of the relative maximum (left hand side) and the height of this relative maximum is shown for all cases.

3 Extension of the 3-Arrhenius Model

This chapter presents the extension of the 3-Arrhenius model and its application for any new fuel. The original model was developed by Weisser [10,19] and further extended during project "Kraftstoffkennzahlen I" (co-funded by the Swiss Federal Office of Energy, grant no. 151786) by Vandersickel [11,20] to account for inert gas effects on ignition delay. The full model is presented below in detail in equations (1) to (3).

$$ln(\tau_1) = \ln(A_2) + \beta_1 ln\left(\frac{p}{p_{ref}}\right) + \left(\frac{T_{A_1}}{T}\right) \quad (1)$$

$$ln(\tau_2) = \ln(A_2) + \beta_2 ln\left(\frac{p}{p_{ref}}\right) + b_2 \ln(T) + \left(\frac{T_{A_2}}{T}\right) + c_2 ln(\Phi) + d_2 ln\left(\frac{[N_2]}{[O_2]}\right) + \left(\frac{[N_2]}{[O_2]}\frac{e_2}{T}\right) \quad (2)$$

$$ln(\tau_3) = \ln(A_3) + \beta_3 ln\left(\frac{p}{p_{ref}}\right) + \left(\frac{T_{A_3}}{T}\right) + d_3 ln\left(\frac{[N_2]}{[O_2]}\right) \quad (3)$$

The parameterization of the original model was based on *measured* shock-tube ignition delay data as follows: first a sensitivity analysis was done to understand the model's dependencies on pressure, air-to-fuel ration and inert gas. Then a linear regression was adopted for the parameterization of the low temperature ignition delay. Finally, a non-linear regression was adopted for the negative temperature coefficient and high temperature ignition delays. The overall procedure did not make use of any optimization tool and required considerable tuning by hand. Furthermore, at best 45 shock-tube experimental operating conditions per fuel were available for the parameterization.

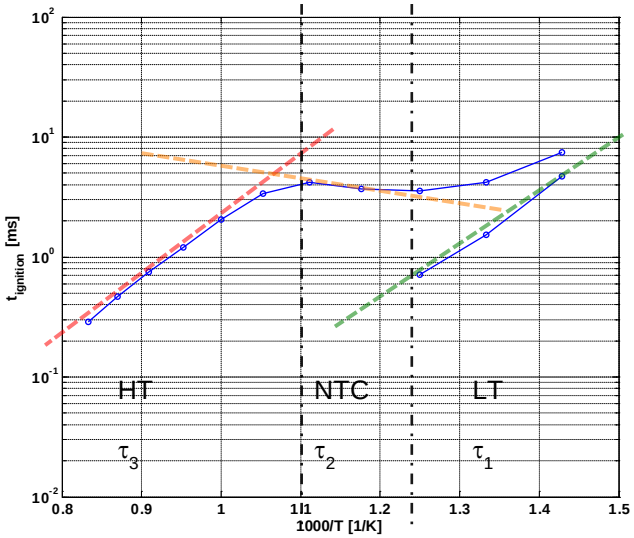

Figure 14 - An exemplary Arrhenius ignition delay plot which includes the linear regression of the three 3-Arrhenius model terms (τ_1, τ_2 and τ_3) onto their corresponding domains LT, NTC and HT. LT: low temperature; NTC: negative temperature coefficient; HT: high temperature.

The current project addresses the abovementioned drawbacks from the previous parameterization process: for the six new fuels RCEM ignition delay was available from [21]. Therefore one could combine a parameter optimization tool, e.g. genetic algorithm, to the ignition integral of Livengood and Wu [12] and parameterize the model. This procedure was tested but encountered two difficulties. Firstly, how does one define an initial guess of the parameters so that the optimization tool can converge towards a global minimum in a reasonable amount of time. Secondly, only 18 operating conditions per fuel were measured in the RCEM, so not a lot of optimization data was available. Due to these difficulties another procedure was developed which allows for a simple parameter initial guess to be made, provides a large database of optimization ignition delay data, and eliminates the need of the ignition integral and therefore reduces optimization times. A final refinement of the 3-Arrhenius model parameters based on RCEM ignition delay data is executed to further improve the predictability of the model. A detailed overview of the entire parameterization procedure and the final refinement is presented below.

3.1 3-Arrhenius Model Parameters' Initial Guess and First Optimization Step

The flow chart of the 3-Arrhenius model parameters' initial guess and first optimization step is shown below in Figure 15. For a completely new fuel, optimization ignition delay data is provided from 0D

adiabatic shock-tube simulations using an existing chemical reaction mechanism for the given fuel. The initial guess of the parameters is provided by a linear regression of the three 3-Arrhenius terms (τ_1, τ_2 and τ_3) onto their corresponding domains of the Arrhenius curve as shown in Figure 14.

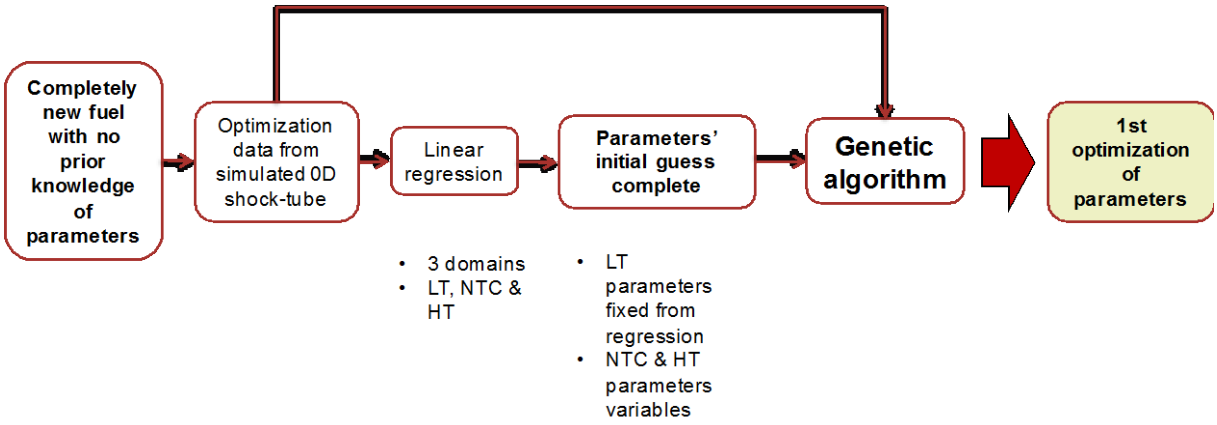

Figure 15 - Illustration of how an initial guess of the 3-Arrhenius Model parameters was made. As a subsequent step a genetic algorithm provides a first optimization step of the model parameters.

The complete numerical expressions of τ_1, τ_2 and τ_3 are shown in equations (1) to (3). Since the low temperature term only has three parameters and can be regressed onto a straight line, the corresponding values from the linear regression were considered final and hence were not modified by the genetic algorithm (GA). It is important to note that this reduces the dimension of the optimization from 14 to 11, which reduces computational time and improves convergence of the GA. The fitness functions of the genetic algorithm were chosen to be the R^2 and $RMSE$ of low and high temperature ignition delay. The latter is logarithmically weighted to balance the importance of all ignition delays over the entire temperature domain. This is important since the s-shaped ignition delay curve can cover multiple orders of magnitude for the given temperature range (cf. Figure 14). Therefore without the logarithmic weighting, discrepancies between modeled and simulated shock-tube ignition delays at the lower temperature domain would result in higher variations in $RMSE$ than the high temperature domain. With the termination of the GA the first set of optimized 3-Arrhenius model parameters is complete. The excellent fitness function values for all fuels is shown in Table 3.

Fuel	LT R^2 and RMSE	HT R^2 and RMSE
***n*-Heptane**	99.7% and 0.07ms	98.0% and 0.2ms
PRF41	99.2% and 0.1ms	97.4% and 0.5ms
TRF7.3	99.7% and 0.7ms	96.6% and 0.4ms
BVP9.1	99.6% and 2.0ms	98.2% and 0.4ms
BVP31.8	99.1% and 0.3ms	98.1% and 0.8ms
***n*-Decane**	99.3% and 0.3ms	98.1% and 0.3ms

Table 3 - Low and high temperature R^2 and RMSE vaules of ignition delay from GA optimization of 3-Arrhenius model in simulated shock-tube data.

However, since this procedure is completely based on simulated optimization ignition delay data the next step is to verify if the first set of optimized 3-Arrhenius model parameters predicts *experimental* ignition delays.

3.2 Validation of the 3-Arrhenius model parameters and refinement based on RCEM experimental data

Figure 16 shows the low and high temperature ignition delays of all fuels over operating conditions; the RCEM experimental data is in light blue. The other colors illustrate ignition delays predicted by the 3-Arrhenius model using the parameters from the first GA optimization, i.e. without refinement. The effects of the variation of the different operating conditions are well captured by the model. However, there is a systematic over-prediction of both low and high ignition delay for all fuels. This is thought to be a consequence of possible thermal stratifications which arise during the compression stroke of the RCEM and which are not accounted for in the shock-tube simulations or the 3-Arrhenius model, since both are 0D. Indeed these findings are in line with the observations reported in [13] by Mitakos et al. Another reason for the model's over prediction of ignition delay could be linked to uncertainties of the chemical reaction mechanisms which were used for the shock-tube simulations. A third and final reason for the discrepancies between model and experiment could be due to the presence of fuel stratification in the RCEM, as is addressed in [22].

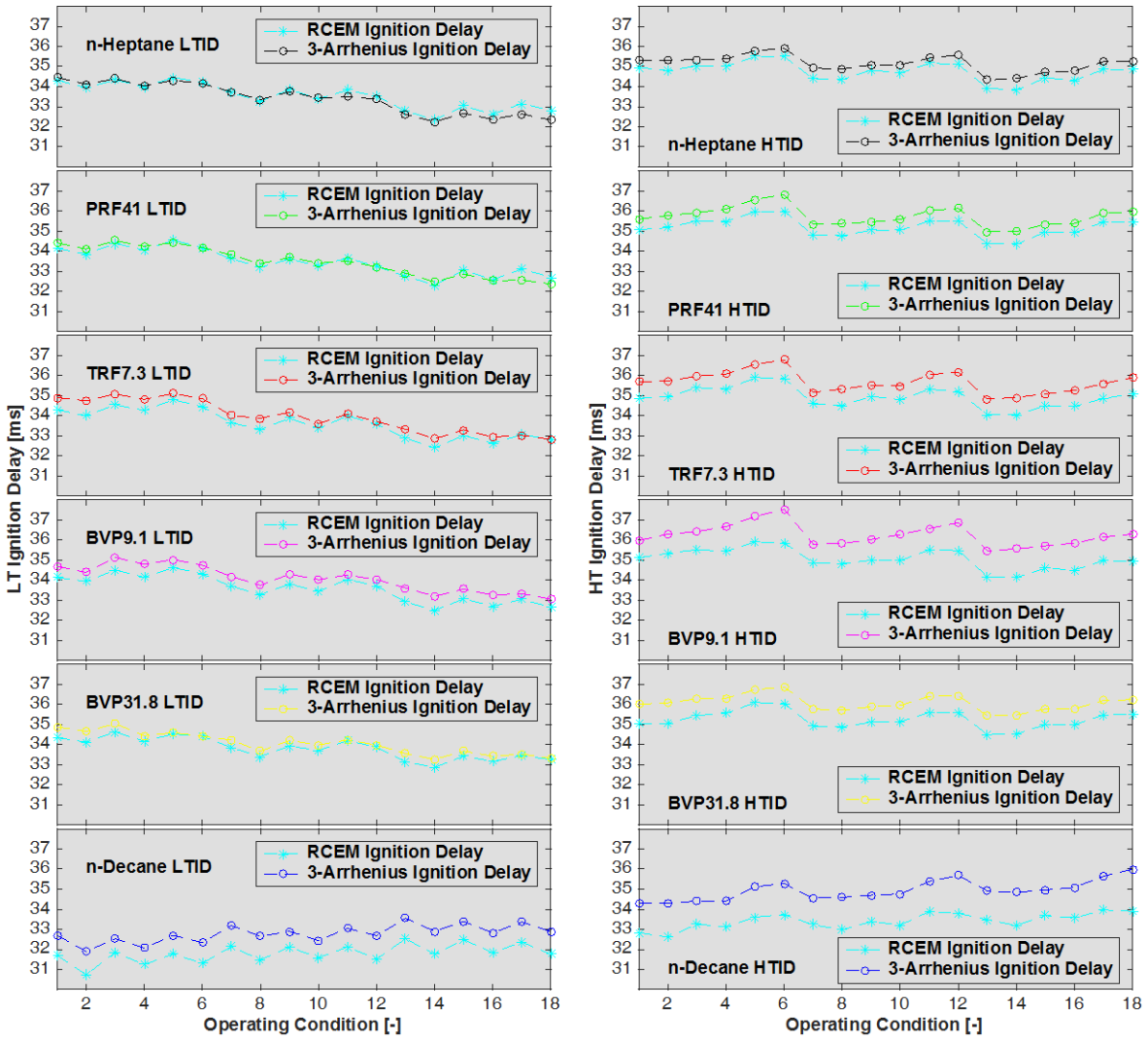

Figure 16 - RCEM and 3-Arrhenus ignition delays vs. operating conditions for parameter sets without refinement. *Left*: low temperature ignition delay (LTID). *Right*: high temperature ignition delay (HTID).

Due to the consistent over prediction of ignition delay and with the goal of making the 3-Arrhenius model predictive for real engine conditions, a final refinement of the model's parameters was carried out to improve its predictive capabilities by means of the RCEM data. As is evident from Figure 16, qualitatively the model is capable of correctly capturing the ignition delay trends over all operating conditions for all fuels. Therefore only a constant offset of low and high temperature ignition delay time is needed to enable the model to become quantitatively predictive. To this end, only the pre-exponential factors A_i of the low and high temperature ignition delay terms were refined (see equations (1) and (3)).

The result of this refinement is shown in Figure 17, where low and high ignition delays are plotted against operating condition for all six fuels. One can now see how the model predicts low and high ignition delay very well.

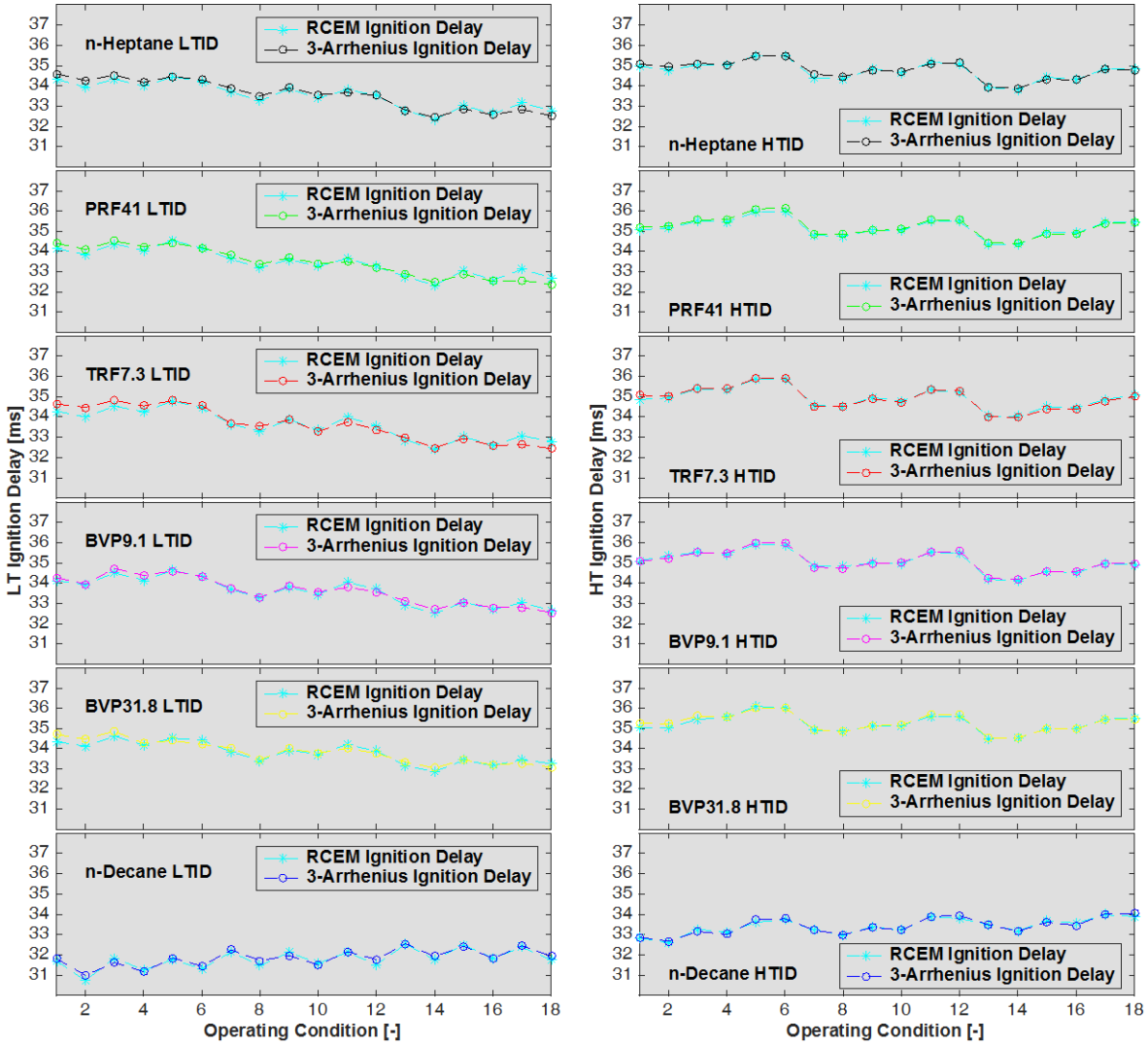

Figure 17 - RCEM and 3-Arrhenus ignition delays vs. operating conditions for parameter sets with refinement of the pre-exponential low temperature and high temperature parameters A_1 and A_3, respectively. *Left*: low temperature ignition delay (LTID). *Right*: high temperature ignition delay (HTID).

Correlation plots in Figure 18 highlight again how well ignition delay is now predicted by the model. Furthermore it is interesting to see that the low temperature ignition delay correlation has a slightly larger spread around the 45° line when compared to the high temperature ignition delay correlation. However

for HCCI combustion applications the main ignition event, i.e. high temperature combustion, is of highest importance and is captured excellently by this retuned model.

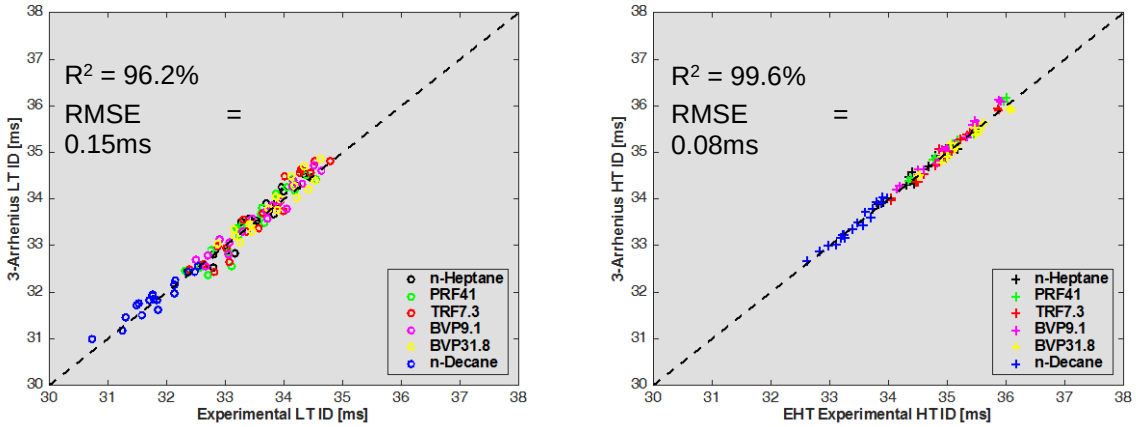

Figure 18 - RCEM vs. 3-Arrhenius low temperature (left) and high temperature (right) ignition delay correlation plot with refinement based on RCEM data.

The final set of retuned parameters with their fitness function statistics is given in Appendix A. The authors believe that the accuracy and simplicity of this model can prove to be a powerful tool for engineers developing HCCI engines.

4 3-Arrhenius/Cool-Flame Model in 0D and 3D-CFD

To date the 3-Arrhenius model was not considered a fully predictive ignition delay model, since e.g. for engine applications it required an experimental pressure and temperature trace up until high temperature ignition delay along which it was integrated according to the ignition integral of Livengood and Wu [12]. With the goal to develop a fully predictive model, it was therefore necessary to model the pressure and temperature trace up until high temperature ignition. This required the inclusion of a low temperature heat release model, i.e. “Cool-Flame Model,” which was developed during this project by Mitakos et al. [13], [23].

ith this model the pressure and temperature rise due to low temperature combustion can be predicted and, together with the 3-Arrhenius ignition delay model, can provide low and high temperature ignition delay predictions. This chapter illustrates the Cool-Flame Model and how it can be combined with the 3-Arrhenius Model into a 0D and 3D-CFD setup to become a fully predictive HCCI combustion model.

4.1 Cool-Flame Heat Release Model

As the name of the model implies, the Cool-Flame Model accounts for the heat release created from low temperature chemical reactions for a HCCI combustion system. It is based on a single Wiebe expression, where the cumulative low temperature heat release Q_{LTR} is defined as follows

$$Q_{LTR}(t) = Q_{LTR,tot} \cdot \left(1 - e^{-a\cdot\left(\frac{t-t_0}{\Delta t_v}\right)^{m+1}}\right) \tag{4}$$

with $Q_{LTR,tot}$ being the total cumulative low temperature heat release, *a* the completeness factor, *m* the form factor, t_0 the low temperature heat release starting time and Δt_v the low temperature heat release

duration. An illustration of the low temperature heat release, the fit of the Wiebe curve and Δt_v are shown below in Figure 19.

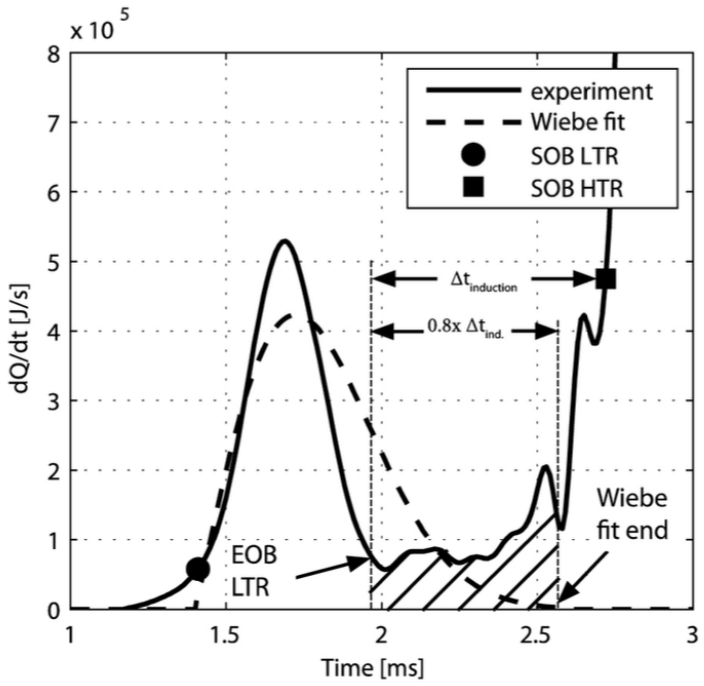

Figure 19 – Illustration of a typical low temperature heat release for a two-stage burning fuel in HCCI combustion. SOB: start of burning; EOB: end of burning; LTR: low temperature heat release; HTR: high temperature heat release.

The two variables which need to be parameterized are $Q_{LTR,tot}$ and Δt_v

$$\frac{Q_{LTR,tot}}{Q_{tot}} = c_0 + c_1 \frac{[inert]}{[O_2]} + c_2 \frac{p_{SOB,LTR}}{p_{ref}} + c_3 \frac{\lambda}{\lambda_{ref}} \tag{5}$$

$$\Delta t_v = b_0 + b_1 \frac{[inert]}{[O_2]} + b_2 \frac{p_{SOB,LTR}}{p_{ref}} + b_3 \frac{\lambda}{\lambda_{ref}} \tag{6}$$

which are a linear function of the total cumulative heat release Q_{tot}, the pressure at start of burning LTR $p_{SOB,LTR}$, the reference pressure p_{ref} (equal to 1bar), the air-to-fuel ratio λ and the reference air-to-fuel ratio λ_{ref} (equal to 1). The variables b_i and c_i are fuel-specific and need to therefore be parameterized according to a linear fit for each fuel.

4.2 Extension of the Cool-Flame Model for All Six Surrogate Fuels

The first step was to prepare the Cool-Flame model for the six surrogate fuels. Therefore the model was parameterized according to the methodology described in [13], [23]. Here two variables need to be parameterized, namely the low temperature heat release duration Δt_v and the cumulative low temperature heat release Q_{LTR}.

	n-heptane	PRF41	TRF7.3	BVP9.1	BVP31.8	*n*-decane
Δt_v						
R^2	93%	93%	93%	96%	79%	94%
RMSE	0.09	0.11	0.11	0.06	0.18	0.08
$Q_{LTR,tot}/Q_{tot}$						
R^2	97%	95%	93%	67%	91%	82%
RMSE x 10^{-2}	0.45	0.64	0.61	1.07	1.46	0.92

Table 4 – Cool-Flame model R^2 and RMSE statistics from parameterization of new fuels.

The outcome of the parameterization is shown below in the two correlation plots (Figure 20) and statistic table (Table 4) of the aforementioned variables. As can be observed, the model is now capable of predicting low temperature heat release duration and cumulative value for all fuels. All model parameters for each fuel can be found in the Appendix.

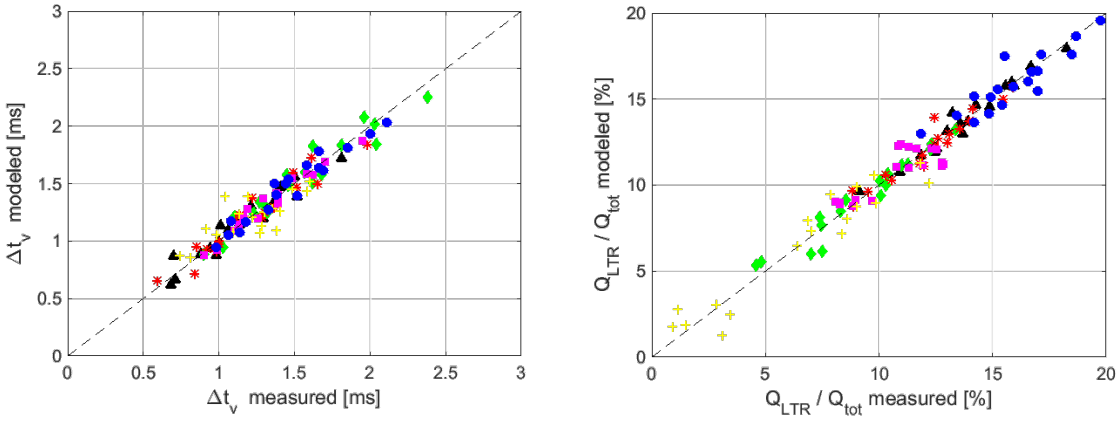

Figure 20 – Left: Low temperature heat release duration correlation plot between RCEM measurements and the Cool-Flame model. Right: Cumulative low temperature heat release correlation plot between RCEM measurements and the Cool-Flame model. The color legend is shown above in Table 4.

4.3 3-Arrhenius/Cool-Flame Model in 0D

Here the 3-Arrhenius auto-ignition model is merged with the Cool-Flame heat release model in 0D to create a fully predictive tool for HCCI combustion ignition delay for a transient system. Figure 21 shows how the 3-Arrhenius and Cool-Flame models work together on a typical 2-stage HCCI combustion transient pressure and temperature trace to predict ignition delays. Starting from an initial pressure and temperature (indicated by the red star) the 3-Arrhenius model is integrated along the pressure and

temperature trace indicated by the red curve. The equation for this curve is derived in equations (7), (8) and (9) from the first law of thermodynamics, assuming all gases are ideal. The heat loss model is a modified Woschni expression for RCEMs from [24].

$$\frac{dU}{dt} = mc_v \frac{dT}{dt} + \underbrace{\left[T\left(\frac{\partial p}{\partial T}\right)_V - p \right]}_{=0 \text{ for ideal gases}} \frac{dV}{dt} = \frac{dQ}{dt} - p\frac{dV}{dt} \tag{7}$$

$$\Leftrightarrow mc_v \frac{dT}{dt} = \frac{dQ}{dt} - p\frac{dV}{dt} \tag{8}$$

with:

$$\frac{dQ}{dt} = -\frac{dQ_{Heat-Losses}}{dt} \tag{9}$$

$$\frac{dQ}{dt} = \frac{dQ_{LTR}}{dt} - \frac{dQ_{Heat-Losses}}{dt} \tag{10}$$

$$\text{and: } \frac{dQ_{LTR}}{dt} = \underbrace{Q_{LTR,tot}\left(1 - e^{-a\left(\frac{t-t_0}{\Delta t_v}\right)^{m+1}}\right)}_{\text{Cool-Flame Model}} \tag{11}$$

Once the low temperature ignition delay term of the 3-Arrhenius model reaches a value of one, low temperature ignition delay (LTID) occurs. At this point in time the Cool-Flame model is activated and releases the low temperature heat release, which subsequently causes an increase in temperature and pressure (indicated by the black curve in Figure 21), which is higher than the red compression curve. This black curve is derived using equation (8) however, as the above equations illustrate, equation (10) now has to account for the Cool-Flame model.

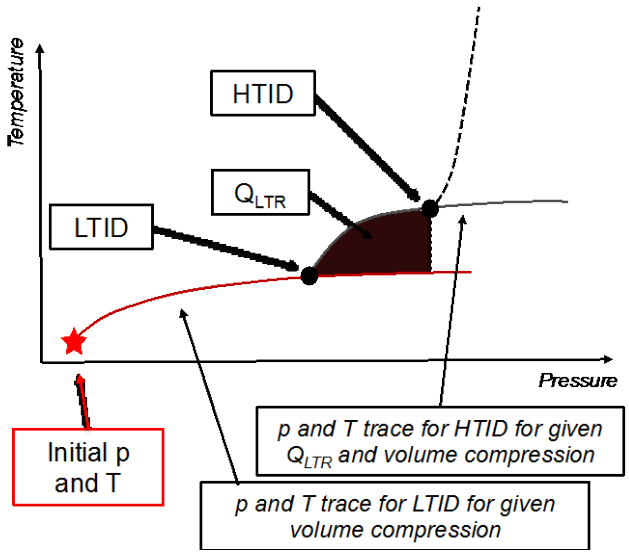

Figure 21 – Illustration of 3-Arrhenius and Cool-Flame models on a p-T trace from HCCI combustion. LTID: Low temperature ignition delay; HTID: High temperature ignition delay; Q_{LTR}: Cool-Flame heat release.

The ignition integral continues to integrate along this new curve until the high temperature ignition integral equals one, i.e. when high temperature ignition (HTID) occurs. After this point, high temperature heat release commences and an abrupt increase in temperature and pressure takes place (illustrated by the black dashed curve). For future reference the 3-Arrhenius and Cool-Flame models in 0D will be simply denoted as the 0D-model.

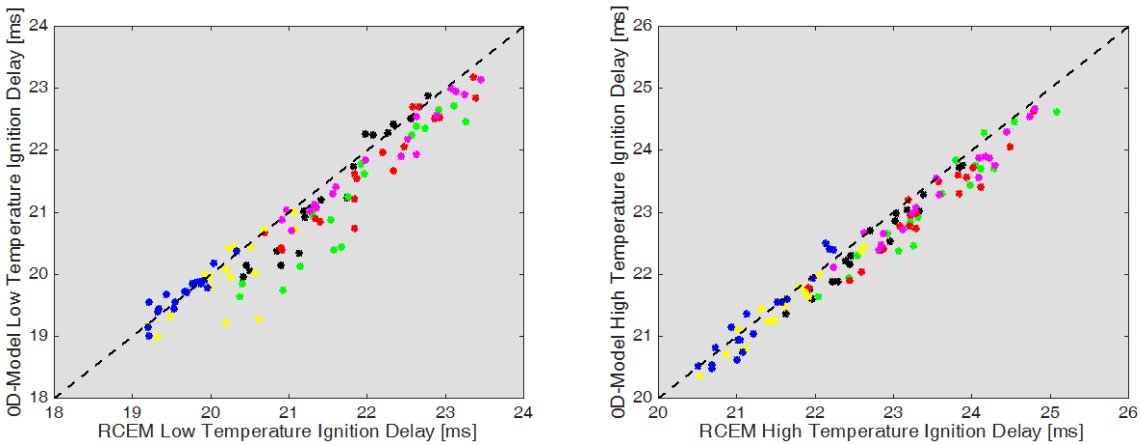

Figure 22 – RCEM experimental vs. 0D-model predicted low (*left*) and high (*right*) temperature ignition delay. The color legend is according to fuel and shown below in Table 5.

The results of the 0D-model low and high temperature ignition delay predictions are shown in Figure 22. R^2 and RMSE values are included in Table 5. There is a very good correlation for all fuels, however with a slight under prediction. This can be associated to uncertainties in the calculation of the heat capacity ratio of the mixture and trapped mass in the crevices. The former was calculated according to the polynomials of Burcat et al. [25]. Here due to the exponential dependency of compression on the heat capacity ratio, a small difference in this term can lead to a large discrepancy in pressure and temperature traces especially up to low temperature combustion. Trapped mass in the crevices was not accounted for in the 0D-model and is known to be around 2% of the total mass at TDC of the RCEM. Both heat capacity and trapped mass studies will be conducted in future work to better understand their effects on the prediction of the 0D-model ignition delays. It is also important to note that the adopted heat loss model [24] could be a additional source for discrepancies. The overall influence of heat capacity ratio, trapped mass and heat losses on the 0D-model will be put into quantitative context in the subsequent chapters.

	n-heptane	PRF41	TRF7.3	BVP9.1	BVP31.8	*n*-decane
Low Temperature						
R^2	95%	90%	90%	96%	63%	85%
RMSE	0.37ms	0.68ms	0.47ms	0.30ms	0.44ms	0.13ms
High Temperature						
R^2	97%	93%	94%	96%	95%	93%
RMSE	0.24ms	0.40ms	0.38ms	0.28ms	0.16ms	0.20ms

Table 5 – R^2 and RMSE of low and high temperature ignition delay for 0D-model compared to RCEM experiment.

4.4 3-Arrhenius/Cool-Flame Model in 3D-CFD

Moving away from 0D modeling and implementing the 3-Arrhenius and Cool-Flame models in 3D-CFD (for future reference this will now be referred to as the 3D-model) can provide valuable information regarding not only ignition delays, but also their location as a consequence of temperature stratifications in the combustion chamber.

The 3D-model was tested by simulating the RCEM on StarCD [26] for *n*-heptane HCCI combustion. Initially the reference case to benchmark the 3D-model was a 3D-CRFD setup of the RCEM using a directly integrated chemical reaction mechanism through the StarCD plug-in DARS-CFD [26]. The reduced chemical reaction mechanism of Tsurushima was used to simulate *n*-heptane chemistry [27]. Here the same 3D-CFD setup was used to simulate both models. The results will therefore show how the 3D-model compares to direct integration (DI) combustion modeling.

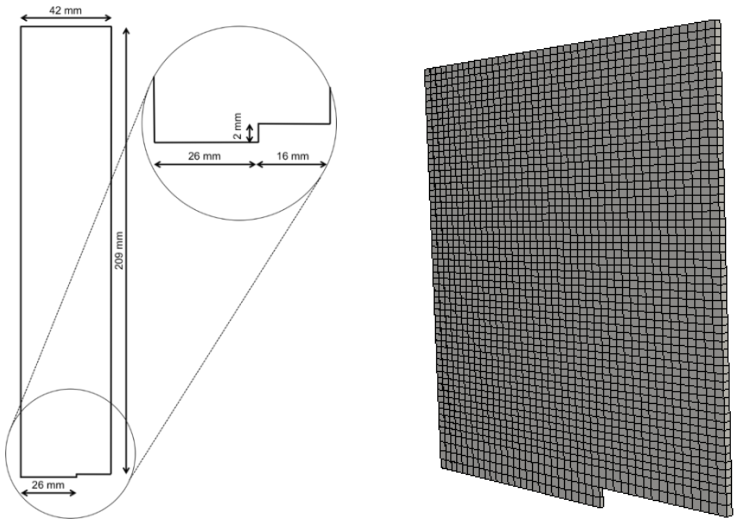

Figure 23 - RCEM geometry without crevices (*left*) and sector mesh of the RCEM (*right*). At BDC a total of 10,704 cells are present.

Both setups used the k-ε high Reynolds number turbulence model. Wall heat losses are computed by the law-of-the-wall, with a fixed wall temperature. The RCEM's geometry and mesh are shown in the figures above. Due to the homogeneity of the mixture one can use a very small opening angle. In this case the sector mesh has an opening angle of 1° which is covered by one cell. The cell size in height and width is roughly 1 mm by 1 mm. The cell count at BDC was roughly 10,000.

18 operating conditions were simulated in total. Their range is shown in the table below.

Fuel	*n*-Heptane
λ	1.25 - 3.5
EGR	0 - 50%
$T_{initial}$	110 - 160°C

Table 6 – 3D-CFD simulation operating conditions.

The integration of the 3-Arrhenius and the cool flame models into the 3D-CFD code is carried out as follows: due to the three dimensionality of the system convection and diffusion of the ignition progress variable between cells needs to be accounted for, i.e. the "transport" of the ignition progress variable needs to be implemented into the CFD code.

As described by Weisser [10], this is done by solving the following transport equation.

$$\underbrace{\frac{\partial\left(\rho C_{ig}\right)}{\partial t}}_{\text{Transient Term}}+\underbrace{\left(\nabla u\right)\rho C_{ig}}_{\text{Convective Term}}=\underbrace{\nabla\left(\rho D\nabla C_{ig}\right)}_{\text{Diffusion Term}}+\underbrace{\frac{\rho}{\tau_{ig}}}_{\text{Source Term}} \tag{12}$$

With the source term's τ_{ig} equal to:

$$\tau_{ig}=\underbrace{\left(\frac{1}{\tau_1+\tau_2}+\frac{1}{\tau_3}\right)^{-1}}_{\text{3-Arrhenius Model}} \tag{13}$$

and:

$$C_{ig}=\frac{Y_l}{Y_{l,ig}} \tag{14}$$

with Y_l equal to a key intermediate specie for ignition and $Y_{l,ig}$ indicates the critical value of this key species. Key intermediate species for low temperature combustion are e.g. hydrogen peroxide and formaldehyde. For high temperature combustion they are e.g. OH radicals and CO. Low temperature ignition occurs once Y_l reaches its critical value $Y_{l,ig}$, i.e. when the ignition progress variable C_{ig} is equal to one. It is important to note however, that C_{ig} can grow to values higher than one. This allows for the ignition progress variable of a certain cell to not only grow due to increases in temperature and pressure, but also through convection and diffusion of the ignition progress variable from adjacent cells which have already ignited.

To avoid unphysical effects of the model, an upper limit of the low temperature ignition progress variable is also necessary. Therefore once the low temperature heat release – provided by the Cool-Flame model and discussed below – has terminated, the low temperature ignition progress variable's growth is blocked. When high temperature ignition is reached, the low temperature ignition progress variable is then set to zero. This choice is motivated by the chemical kinetics of low, intermediate and high temperature combustion [28]: during low temperature heat release there is a rapid growth of key intermediate low temperature species. When the low temperature heat release terminates, this growth plateaus. When high temperature ignition occurs, a rapid consumption of the key intermediate low temperature species takes place. Therefore since the low temperature ignition progress variable is directly proportional to the key intermediate species of low temperature combustion, the occurrence of high temperature combustion means it should also be reduced to zero.

A limit for the high temperature ignition progress variable needs to also be implemented into the model, e.g. once high temperature heat release is terminated (all the fuel in the cell is depleted), then set the high temperature ignition integral value to zero. For this to be implemented one first needs to develop a high temperature heat release model for HCCI combustion. This is currently being investigated and the authors expect first results in the next six months.

The enthalpy equation (15) is used to implement the Cool-Flame model into the 3D-CFD code. Similar to transport equation (12), one needs to account for interactions between cells. Therefore convection, diffusion, pressure and stress terms for the transportation of enthalpy are present.

$$\underbrace{\frac{\partial\left(\rho h\right)}{\partial t}}_{\text{Transient term}}+\underbrace{\frac{\partial}{\partial x_j}\left(\rho h u_j+F_{h,j}\right)}_{\text{Convection and diffusion terms}}=\underbrace{\frac{\partial p}{\partial t}+u_j\frac{\partial p}{\partial x_j}}_{\text{Pressure terms}}+\underbrace{\tau_{ij}\frac{\partial u_i}{\partial x_j}}_{\text{Stress term}}+\underbrace{s_h}_{\text{Source term}} \tag{15}$$

with the source term s_h equal to the low temperature heat release, i.e. the Cool-Flame model.

$$s_h = \dot{Q}_{LTR} = Q_{LTR,tot}\left(1 - e^{-a\left(\frac{t-t_0}{\Delta t_v}\right)^{m+1}}\right) \quad (16)$$

The complete methodology behind the integration of the two models in 3D-CFD is shown in the two flow charts below. The first flow chart (Figure 24) applies for low temperature ignition, while the second chart (Figure 25) covers high temperature ignition. The simulation setup is of a typical engine cycle, starting e.g. from BDC.

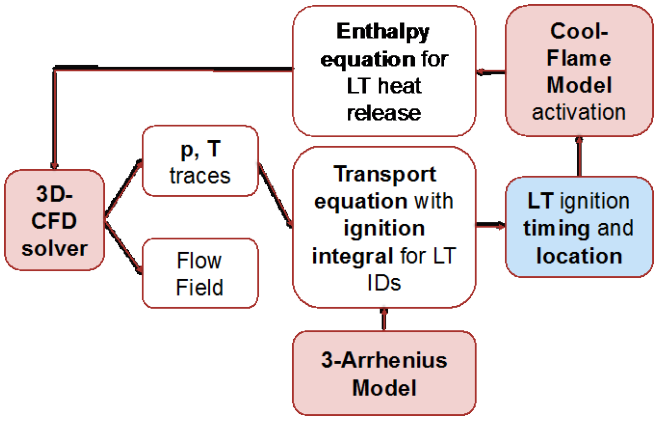

Figure 24 – 3D-model low temperature ignition flow chart. p: pressure; T: temperature; LT: low temperature; ID: ignition delay.

Figure 24 starts from the 3D-CFD solver which computes flow field and thermodynamic variables. Starting from BDC, the compression of the mixture causes a rise in pressure and temperature. Through the transport equation, the low temperature ignition integral with the 3-Arrhenius model is integrated along the pressure-temperature trace of every single cell in the domain. When the low temperature ignition progress variable reaches a value of one for a certain cell, low temperature ignition takes place and enthalpy sources (equation (16)) from the Cool-Flame model are activated in the enthalpy equation (15) representing the heat release of the low-temperature chemistry.

Figure 25 illustrates the high temperature ignition path. Once a certain cell has gone through low temperature ignition, the pressure and temperature trace provided by the 3D-CFD solver includes an enthalpy increase due to LTR. The high temperature ignition progress variable is integrated along this pressure and temperature trace. When it reaches its critical value of one high temperature ignition occurs in that cell.

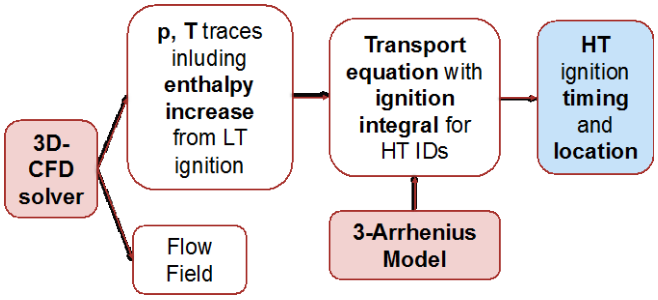

Figure 25 – 3D-CFD 3-Arrhenius and Cool-Flame high temperature ignition flow chart. p: pressure; T: temperature; LT: low temperature; HT: high temperature; ID: ignition delay.

Figure 26 shows a correlation plot between low and high temperature ignition delay of the 3D-CFD/DI and 3D-model simulations: while excellent correlation between the two approaches is evident (high R^2 values for both high and low-temperature delays), the 3D-model slightly under predicts ignition delays. It is however important to mention that the 3D-model took 15 minutes to simulate on one processor, while the 3D-CFD/DI simulation took 1.5-2 hours to simulate on 4 processors. Therefore, a speed-up factor of 32 can be achieved with the 3D-model for very comparable ignition delay predictions.

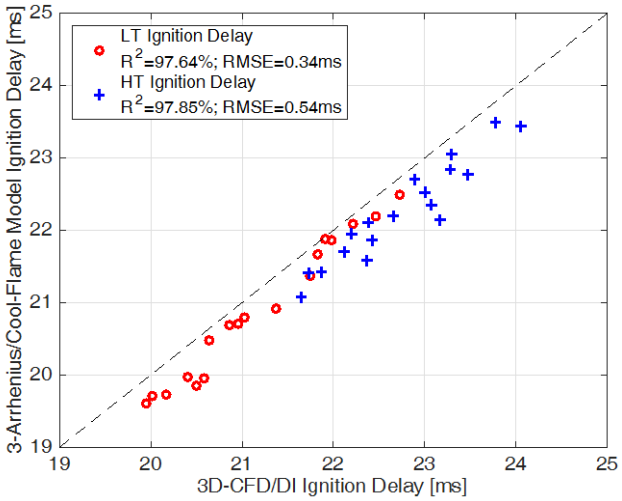

Figure 26 – Low (*red*) and high (*blue*) temperature ignition delays of 3D-CFD/DI vs. 3D-model simulations.

Comparing the 0D-model and the 3D-model to the experimental RCEM ignition delay data (Figure 27 and Figure 28) one can see how both models can correctly capture ignition delay trends, but slightly under predict those values. As mentioned before these small discrepancies can be caused by trapped fuel-gas mixture in the RCEM's crevices, which is not modeled in 0D or 3D. The exact fuel-gas composition could also slightly deviate between simulation and experiment, therefore influencing the heat capacity ratio. Another motive could be the employed heat loss models.

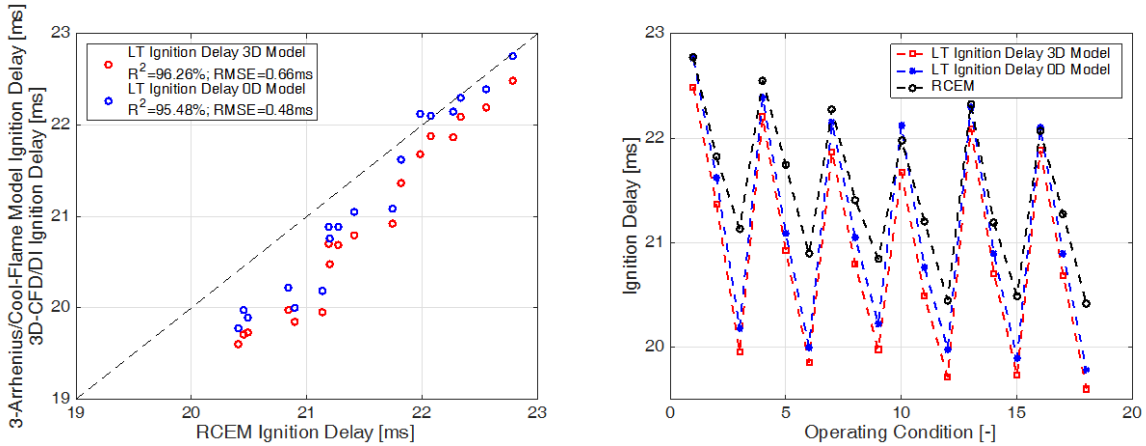

Figure 27 – Correlation plot (*left*) between the 0D-model, 3D-model and experimental RCEM <u>low</u> temperature ignition delay. On the *right* all ignition delays are plotted against operating condition.

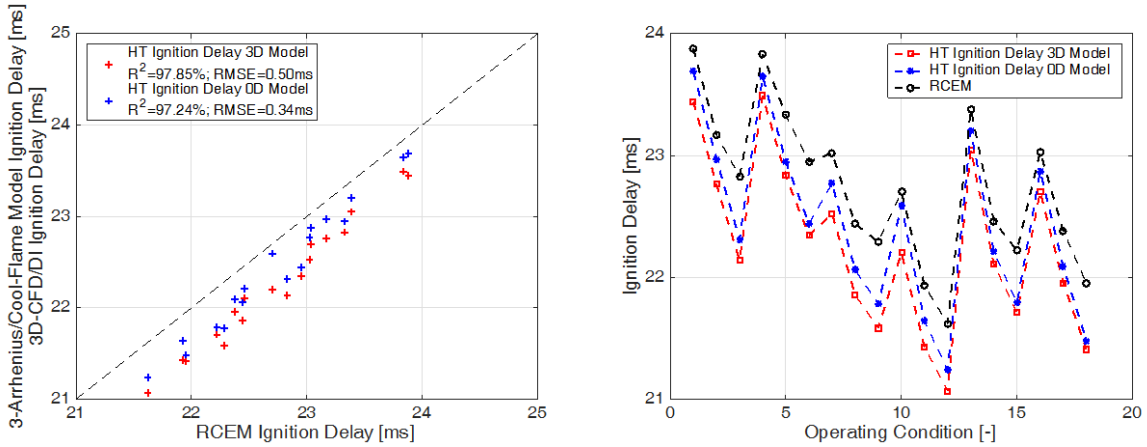

Figure 28 – Correlation plot (*left*) between the 0D-model, 3D-model and experimental RCEM high temperature ignition delay. On the *right* all ignition delays are plotted against operating condition.

To put these aspects into a clearer perspective and to see how they influence the predicted compression-combustion stroke, the pressure and temperature curves of operating condition $\lambda = 1.85$, EGR 25% and $T_{Initial}$ = 110°C (also seen as the third operating condition in figures 25 and 26) are shown in Figure 29. When compared to the RCEM experimental data both the models reach higher pressures and temperatures earlier on in the compression stroke. This causes low temperature ignition to be reached earlier. This also influences the modeled low temperature heat release. Equation (4) of the Cool-Flame model shows it is a function of total cumulative low temperature heat release ($Q_{LTR,tot}$) and its duration Δt_v. As shown in equations (5) and (6) both of these variables are a function of EGR, low temperature ignition pressure and air-to-fuel ratio. Since the mixture is highly homogeneous EGR and λ do not vary significantly during compression. The dominating variable is $p_{SOB,LTR}$, which in the 0D-model and 3D-model is lower than the experiment (c.f. Figure 29).

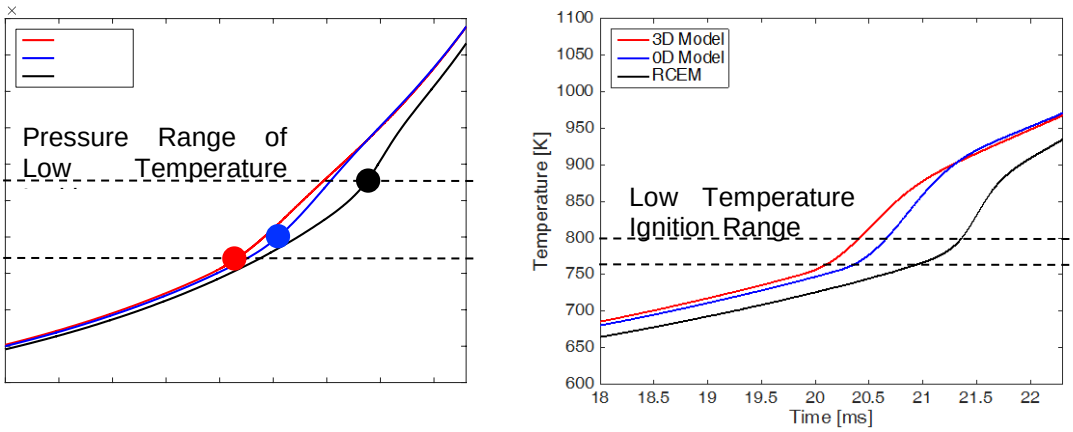

Figure 29 – Pressure (*left*) and temperature (*right*) plots of compression and combustion over time of the 0D-model, the 3D-model and the RCEM experiment. Low temperature ignition pressure and temperature ranges are also indicated. The colored dots indicate low temperature ignition pressures.

Parameters c_2 and b_2 are positive and negative, respectively. Therefore for lower low temperature ignition pressures $Q_{LTR,tot}$ and Δt_v will predicted smaller and larger, respectively. Thus it is fundamentally important to correctly predict the compression stroke up until low temperature ignition, especially due to the high sensitivity of HCCI ignition on temperature. Further effort will be invested to try to correct the modeled compression strokes to improve the 0D-model's and 3D-model's overall predictability. Thereafter all fuels and all operating conditions will be simulated again with the 0D- and 3D-model.

However it is very important to note that even now the predictability of both models is very high and always at a very low computational demand.

5 Partially-Premixed Charge Compression Ignition

This work package seeks to investigate combustion strategies with a large degree of premixing of the fuel prior to ignition, usually achieved by several short injections – with injection timings and quantities carefully chosen so as not to undergo high-temperature ignition – before the main ignition. Such approaches allow for heat-release shaping and enable very low engine-out emission levels. A brand new Daimler OM642 engine was installed at the IVK in Stuttgart in the co-funding project FVV "Kraftstoffkennzahlen II" to provide the experimental data. Due to complications during its commissioning, no PCCI investigations could be provided for validation. Towards developing a model for PCCI combustion, an initial investigation has hence been performed in this work package using experimental data of a split injection setup reported in the literature by Skeen at al. [15], obtained in the optically accessible combustion vessel installed at Sandia. The study reports data for the so-called "Spray A" with split injection (0.5ms injection – 0.5ms dwell – 0.5ms injection) for various initial conditions (temperature, pressure and oxygen content). Two conditions are representative of PCCI-like combustion with a low reactivity environment while the third corresponds to a 'classical' diesel combustion with high initial temperature and pressure. The idea was to first validate the split injection setup with a combustion model at high temperature and pressures and then move towards the PCCI-like combustion setups. Concerning combustion modeling, two approaches are available: the first one is to use the so-called "direct integration" (DI), where the chemical source terms in the species transport equations are obtained from Arrhenius type rate expressions which are evaluated using the Favre averaged temperature and species mass fractions and in every CFD cell. This technique has become quite popular in the combustion community (e.g. see [29–31]), since it allows for inclusion of detailed chemical kinetics and multiple fuels. The methodology however comes at a high computational cost since in addition to mass, momentum and energy, transport equations for all species are also directly solved in every CFD cell at every time step. Furthermore, turbulence-chemistry interaction is completely disregarded by this approach, which from a fundamental perspective cannot be neglected since some of the time-scales of flow and chemical kinetics show considerable overlap. A second approach has therefore also been followed using the Conditional Moment Closure (CMC) combustion model which has seen successful application to sprays and Diesel engines in previous studies [32–49]. CMC exploits the fact that conditional quantities show considerably lower spatial variation than their unconditional counterparts, hence the CMC equations can be solved on a considerably coarser grid than the CFD mesh, which significantly reduces the computational effort. Additionally, the CMC approach captures the interaction between turbulent fluctuations and chemical reactions, which makes it superior to DI when simulating sprays and is therefore the recommended approach for these types of setups. Indeed in Bolla et al. [50] and Pandurangi et al. [44] it is highlighted that CMC is highly suitable to model both 'classical' diesel combustion as well as low-temperature combustion (LTC) where long ignition delays are present. The latter are very similar to PCCI conditions in that a large extent of premixing occurs prior to ignition due to lower reactivity of the ambient surrounding. For the split injection investigation, the authors therefore opted for CMC combustion model. Furthermore, with the goal of simulating more than two injections as is often the case in PCCI combustion, the CMC code was extended to n-injections (please refer to [51] for more information).

Initially a non-reactive flow field simulation was run to calibrate the spray. First a Reynolds-averaged Navier-Stokes (RANS) simulation using the k-ϵ turbulence model was employed. More details regarding the numerical setup can be found in [52]. The vapor penetration length was compared to the experimental data and plotted against time as seen in Figure 30.

Solid curves indicate the first injection while dashed curves the second. The black curve is the experiment's. The yellow and light blue spread around these curve indicates the standard deviation. All the other colored curves are simulations with different spray and turbulence setups. The simulation indicated by the magenta curve used the turbulence mixing constant $c_{\epsilon 1} = 1.51$. Since the simulation under predicted spray penetration, the mixing constant was increased to $c_{\epsilon 1} = 1.53$, which resulted in the blue line. This still results in an under prediction until roughly 1 ms after start of injection. However

the time from 1 – 2 ms is mostly accurate for the first injection. The Kelvin-Helmholtz and Rayleigh-Taylor droplet break-up model was also tested and shown as the yellow curve. An 0.5 ms simulation time sufficed to see that this model did not improve predictions.

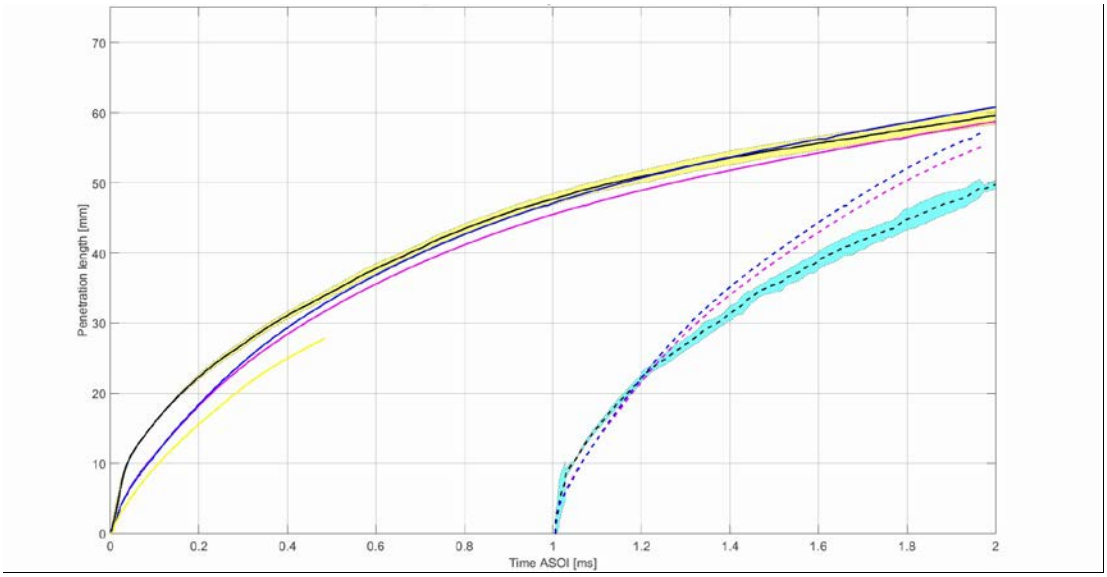

Figure 30 – Comparison of the non-reactive fuel vapor penetration length of RANS with Reitz Diwakar (R-D) atomization and different droplet break-up models.

Concerning the second injection, the model must be able to account for the slip-stream effect of the first injection, i.e. a low density zone trailing the first injection which in turn will cause the second injection to penetrate faster into the combustion chamber. However trying to enhance mixing of the first spray and keeping these setting constant also for the second spray causes a complete overshoot of the second spray. This leads to the conclusion that for transient split injection setups RANS is not sufficiently accurate to predict the flow field. Nevertheless this does not hint that RANS is an overall bad model for diesel-type spray predictions. Indeed is has been successfully used numerous times in the past [21], [33,52]. Furthermore it is important to note that for a *single* injection setup of Spray A with long injection durations, RANS can correctly predict non-reactive penetration lengths [53]. Therefore it is possible that for this split injection setup individual tuning of each injection could lead to better results. Another option is using a large eddy simulation (LES) to solve the flow field. Instead of a time/ensemble averaged flow-field, as is the case in RANS, LES explicitly solves large scale eddies, while sub-grid scale eddies, which are considered more universal, are modeled. Therefore the turbulent spray is described much more in detailed, and consequently any interaction with combustion will also be captured more in detail. Given the transient nature of this setup, the complex interactions between first and second spray, and their subsequent important interaction with combustion, the authors decided to opt for a more elaborate description of turbulence with large eddy simulations (LES).

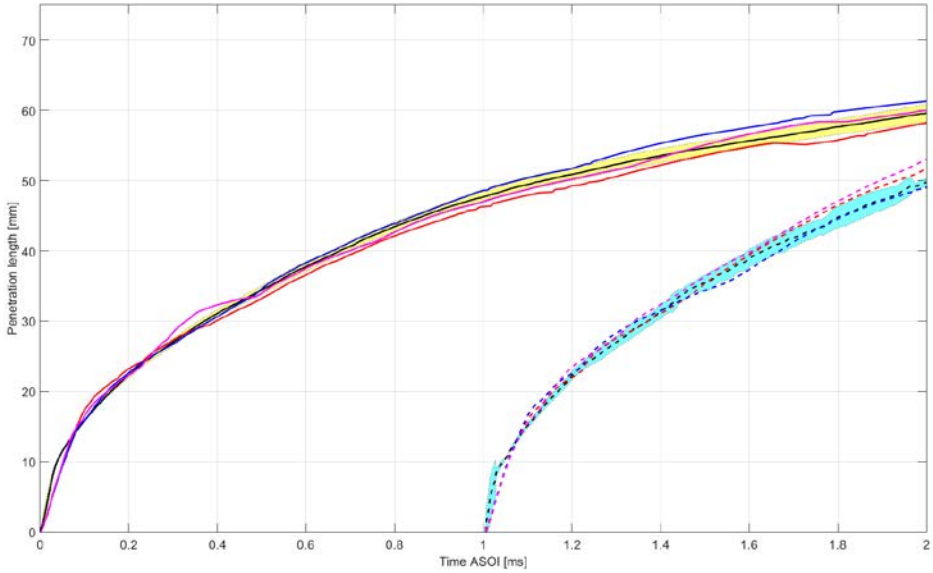

Figure 31 - Comparison of the non-reactive fuel vapor penetration length of LES with Reitz Diwakar (R-D) atomization and Kelvin-Helmholtz & Rayleigh-Taylor droplet break-up model.

Therefore the turbulence model of the flow field solver Star-CD was changed to LES (Large Eddy Simulation). More information about the numerical setup can be found in [54]. The non-reactive simulation was repeated and led to the result visible in Figure 31. Again the solid lines indicate first injection while the dashed the second. In black are the experimental data with yellow and light blue indicating their standard deviations. The colored lines represent three simulations using identical settings, but since LES shows cycle-to-cycle variations one also sees different penetration lengths. All simulations predict spray tip penetration lengths of both first and second injection in very close agreement with the experiment. Furthermore, the so-called slipstream effect occurring during the second injection is predicted very well.

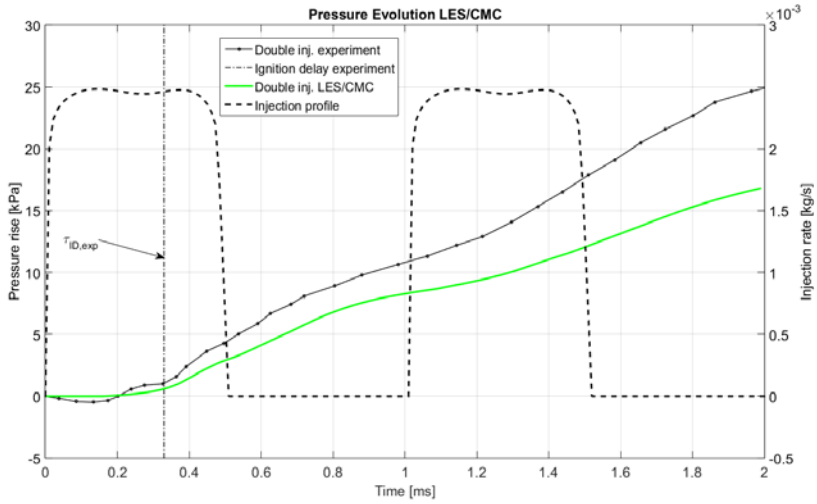

Figure 32 - Pressure rise over time of the split injection experiment and the LES/CMC simulation. Injection profile over time is also included.

With the spray correctly calibrated, the next step was to simulate a reactive setup. When using the LES flow field solver, which applies a filter for sub-grid scale modeling, the CMC combustion model requires that the equations are solved for conditionally filtered reactive scalars, with the conditioning being on

mixture fraction. These filtered equations have been widely used by the combustion community and can be found e.g. in [48,49,55–60]. The n-dodecane chemical reaction mechanism, which importantly includes low temperature chemistry reactions for PCCI combustion, was developed by Yao et al. [17] and comprises 54 species.

Very first results of the split injection for diesel-like conditions of pressure rise in Figure 32 show ignition delay is correctly captured. The plot also shows the split injection profile. Interestingly, after second injection there is a clear period where the injected mass evaporates, leans out and then ignites. A quantitative comparison between experiment and simulation pressure rise rate shows that the latter is lower, but the trend is correctly captured. It is important to note that this is pressure rise rate and not pressure, therefore the absolute error is of only 0.08 bar over an initial pressure of 60 bar. The reason behind this small difference in magnitude is thought to be due to marginal differences in total volume of the modeled and actual combustion chamber, which includes various measurement instrumentation in its volume.

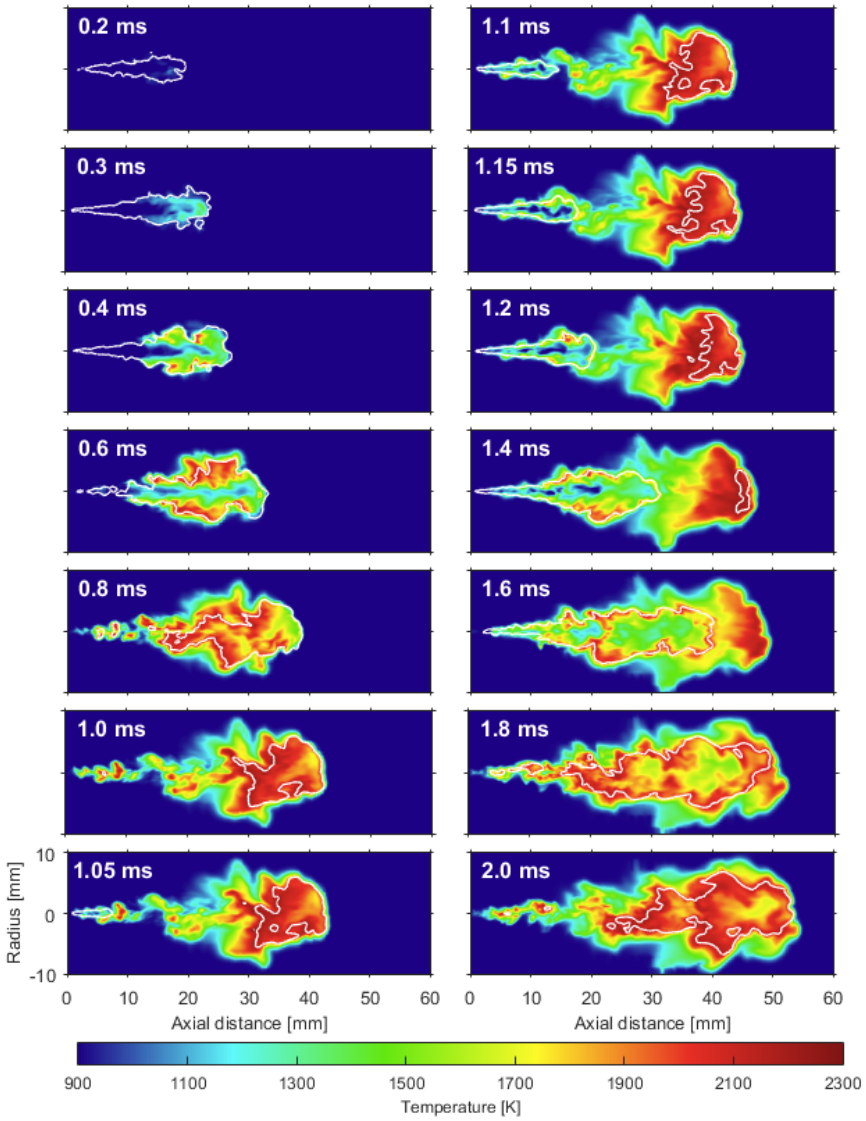

Figure 33 - Instantaneous non-averaged temperature contour plot over time of LES/CMC split injection. Shorter time intervals are shown at the start of second injection to show more in detail the interaction between first and second injection. The white lines indicate the stoichiometric mixture fraction.

Instantaneous non-averaged contour plots of temperature in Figure 33 and OH mass fraction in Figure 34 show that the ignition spots of the first injection start on the side of the spray and move downstream towards the tip and upstream towards the injector. In the case of a longer injection, the flame would stabilize at the lift-off length, here, the injection ends before a stable lift-off length is achieved. The second injection also ignites on the side at around 1.2 ms (c.f. ignition of second injection in Figure 32) and then moves downstream and merges with the reaction zone of the first injection at around 1.8 ms. It is also interesting to see how LES/CMC correctly captures what Knox et al. [61] refer to as “combustion recession.” This is the process when a lifted flame progresses upstream towards the near-injector region after the end of the injection, which can clearly be seen after the first injection between 0.6 and 0.8 ms, and again after the second injection between 1.6 and 1.8 ms. These findings are in accordance with the experiment as shown in the Schlieren images of Figure 35.

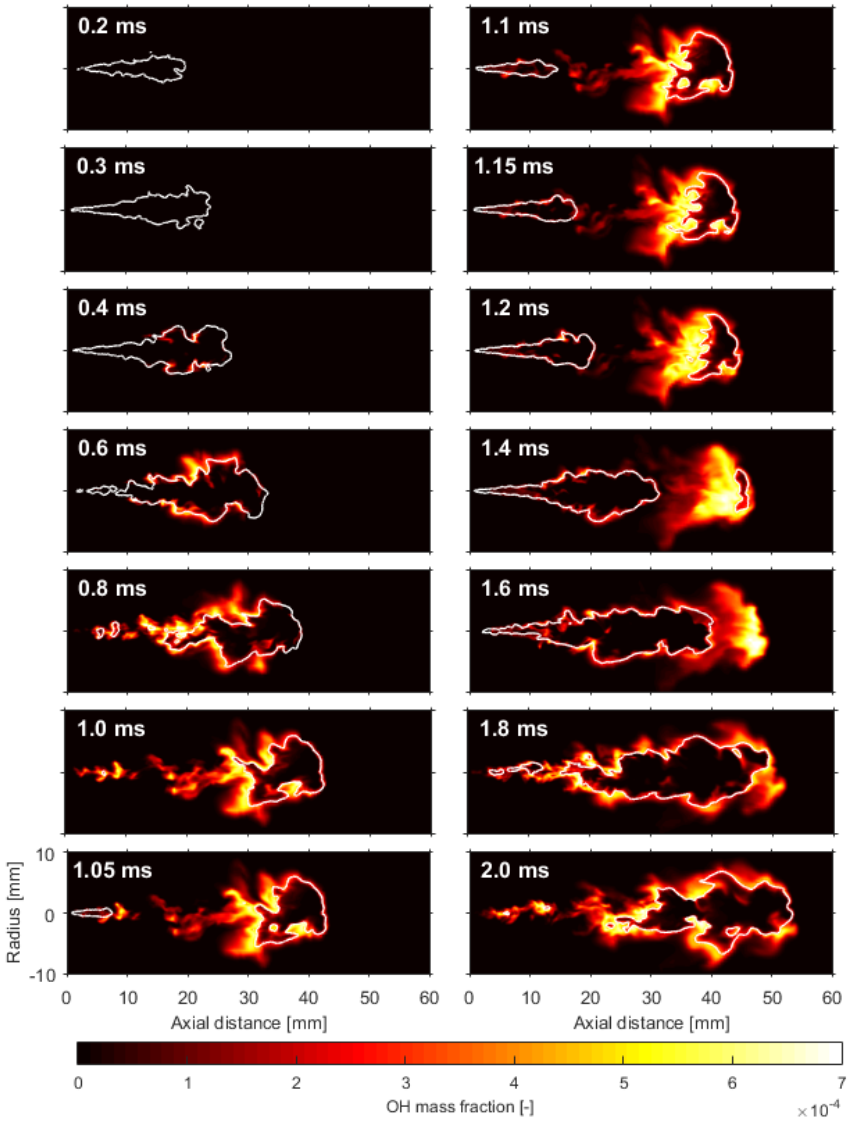

Figure 34 - Instantaneous non-averaged OH mass fraction contour plot over time of LES/CMC split injection. Shorter time intervals are shown at the start of second injection to show more in detail the interaction between first and second injection. The white lines indicate the stoichiometric mixture fraction.

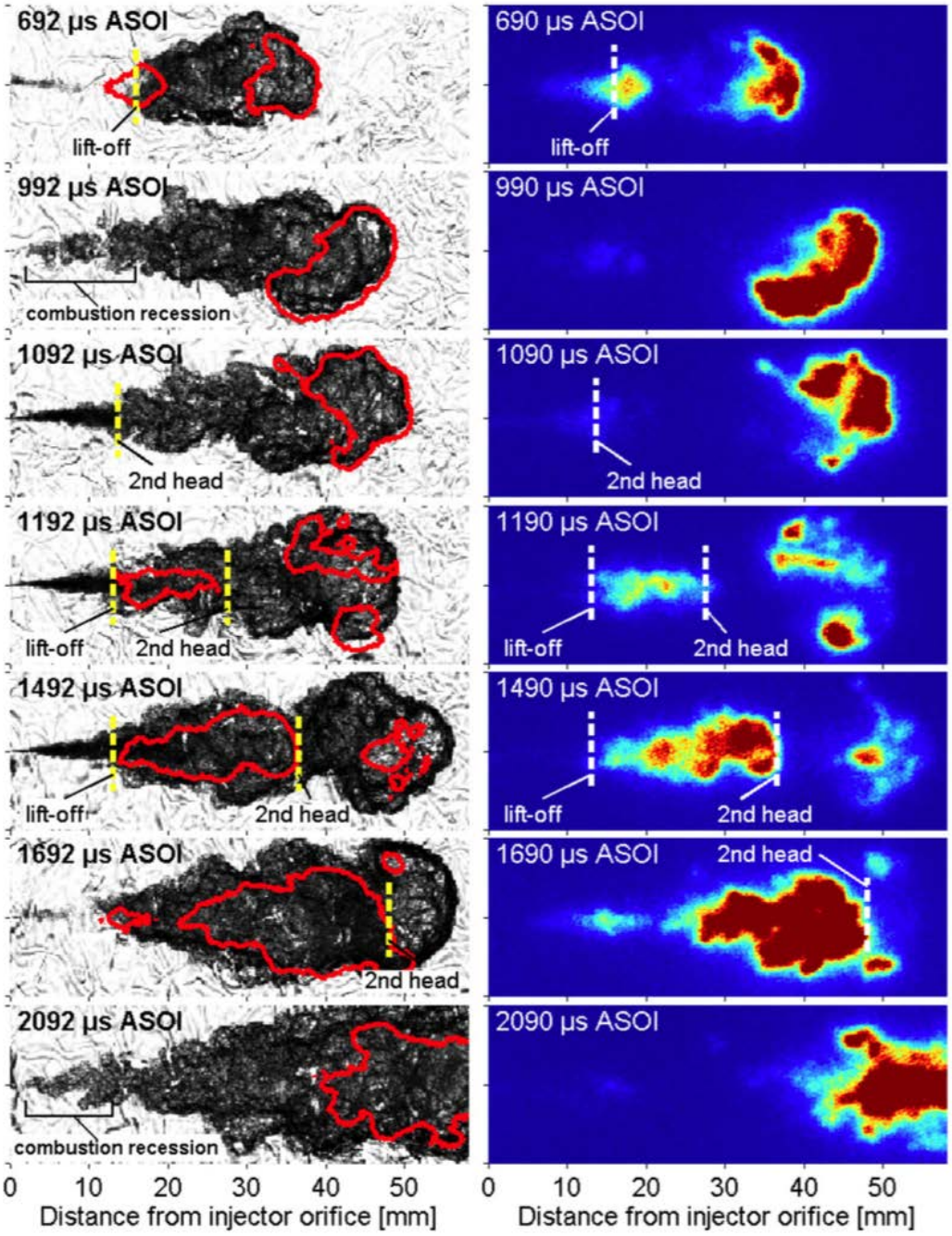

Figure 35 - Time sequence of schlieren and formaldehyde PLIF images of split injection experiment. Dashed lines are provided to indicate the lift-off location and the vapor penetration distance of the second jet. Red lines overlaid on the left are borders from the 355-nm PLIF at the right. Figure taken from Skeen at al. [15].

Future simulations are planned for the same split injection setup as above to gather statistical data for averaging which will permit a more detailed comparison to experimental data. Furthermore PCCI split injection cases will also be simulated. Here ignition occurs after the end of the first injection due to lower reactivity, which can be achieved by lowering the ambient temperature or decreasing the oxygen content (corresponding to EGR). Correctly predicting the prolonged ignition delay will constitute an essential validation of the PCCI LES-CMC model. The CMC model has already shown very good predictive

capabilities in conjunction with RANS for single injections in numerous spray bombs of varying sizes both for *n*-heptane and *n*-dodecane sprays [34–39]. Engine studies are also reported using CMC for single injections [36,40–43] in a RANS context for very wide ranges in operating conditions, viz. low reactivity conditions due to very high EGR rates or low end of compression temperatures with early injection or extreme Miller valve timings. Multiple injections scheduling using either pilot injection [44] or post-injections [45–47], are also reported using RANS turbulence treatment with the CMC combustion model.

For LES-CMC, early applications of the in-house code were reported for spray rigs using *n*-heptane and *n*-dodecane in [48,49] and further application of this platform using the developed extensions for multiple injections to study PCCI is highly promising.

6 Conclusions

This project investigates the appropriateness of the Cetane Number (CN) as an index for combustion of automotive fuel blends with and without oxygenates during HCCI combustion. To this end, the fuels have been characterized experimentally in engines (at IVK Stuttgart) and six surrogates with identical CN in a Rapid Compression Expansion Machine (RCEM) at ETH Zurich. The optical analysis in the RCEM revealed an auto-igniting propagation front traveling slightly slower than the speed of sound, demonstrating a high degree of homogeneity of the mixture in the RCEM. Furthermore, in accordance to the findings of IVK, the thermodynamic analysis shows a clear low and high temperature ignition temperature range for all fuels. The time needed to reach the low temperature ignition range is a function of fuel ignition quality (i.e. clearly correlates with CN) and charge state. The same holds true for high temperature ignition, but the effect of CN was less evident. Furthermore an important contribution towards high temperature ignition is the cool-flame heat release. This emphasizes the importance of the developed Cool-Flame heat release model.

New 3-Arrhenius and Cool-Flame model parameterization methodologies were successfully developed and applied to the project's surrogate fuels showing excellent agreement with the RCEM experimental data in terms of ignition delays and low temperature heat release. The parameterization methodologies are based on a genetic algorithm, which can be applied to any type of optimization data stemming either from shock-tubes or engine-like data. The initial guess of parameters – based on either detailed kinetic schemes or on experiments in shock tubes – is shown to be of high importance to reduce optimization times and assure convergence towards a good set of optimized parameters. By combining the 3-Arrhenius model and the Cool-Flame model with an ignition integral approach (Livengood-Wu), a fully predictive methodology for low and high temperature ignition delays has been established, which can be used in both 0D- and 3D-simulations. Both approaches can be used as stand-alone HCCI combustion simulation tools with varying degrees of complexity and predictive capabilities, always at a low computational cost (e.g. the 3D-model is 100 times faster than a 3D-CFD simulation in conjunction with reduced chemical kinetics). Both 0D and 3D models showed very good predictive capabilities with respect to low and high temperature ignition delays in the RCEM.

Towards PCCI combustion, a study of a split-injection setup with experimental data available from literature was carried out: RANS and LES flow-field solvers were coupled with a Conditional Moment Closure (CMC) combustion model and simulations were carried out for two cases, i.e. one at a diesel-like condition and one at a low temperature combustion condition. Ignition delays were predicted well by both numerical methods, as were flame structures. As expected, LES-CMC showed greater detail in the flame structure and also correctly predicted a full combustion recession after first and second injections. To conclude, RANS- and LES-CMC both show significant promise for modeling and understanding the complicated mechanisms involved in highly transient multiple injection combustion systems representative of PCCI combustion in engines with state of the art injection schedules.

7 Outlook

7.1 3-Stage Heat Release Model for HCCI Combustion

A current modeling development at LAV is to extend the Cool-Flame heat release model, so that it also includes intermediate and high temperature heat releases. A schematic of the contribution of each heat release (i.e. low, intermediate and high) is shown on the heat release rate plot in Figure 36. This is seen as a key advancement to develop a *complete* HCCI combustion model in 3D-CFD that is compact and fast. To reach this goal the 3-Stage heat release model will be merged with the 3-Arrhenius auto-ignition model, in a similar fashion to the 3D-model described above.

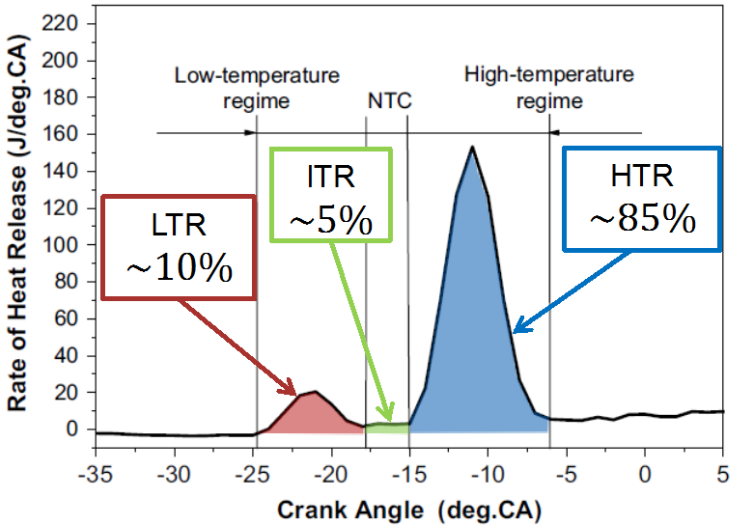

Figure 36 - Exemplary HCCI combustion heat release rate plot with the individual contributions from low (LTR), intermediate (ITR) and high (HTR) temperature combustion. Figure taken from Yao et al. [62].

8 Dissemination of results

8.1 The following publications have been published during this project:

- D. A. Mitakos, C. Blomberg, A. Vandersickel, Y.M. Wright, B. Schneider, K. Boulouchos, "Ignition Delays of Different Homogeneous Fuel-air Mixtures in a Rapid Compression Expansion Machine and Comparison with a 3-Stage-ignition Model Parameterized on Shock Tube Data", *SAE Int. J. Engines **6** (4), 1934-1952*, 2013.
- D. A. Mitakos, C. Blomberg, Y. M. Wright, P. Obrecht, B. Schneider, and K. Boulouchos, "Integration of a Cool-Flame Heat Release Rate Model into a 3-Stage Ignition Model for HCCI Applications and Different Fuels," *SAE Technical paper No. 2014-01-1268*, 2014.
- K. Steurs, C. K. Blomberg, and K. Boulouchos, "Knock in an Ethanol Fueled Spark Ignition Engine : Detection Methods with Cycle-Statistical Analysis and Predictions Using Different Auto-Ignition Models," *SAE Int. J. Engines **7** (2), 568–583*, 2014.
- K. Steurs, C. Blomberg, and K. Boulouchos, "Formulation of a Knock Model for Ethanol and Iso-Octane under Specific Consideration of the Thermal Boundary Layer within the End-Gas," *SAE Int. J. Engines **7** (4), 1752–1772*, 2014.
- C. Blomberg, D. Mitakos, M. Bardi, K. Boulouchos, Y. M. Wright, and A. Vandersickel, "Extension of the Phenomenological 3-Arrhenius Auto-Ignition Model for Six Surrogate Automotive Fuels," *SAE Int. J. Engines **9** (3)*, 2016.
- C. Blomberg, L. Zeugin, S. Pandurangi, M. Bolla, K. Boulouchos and Y. M. Wright, "Modeling split injections of "Spray A" using a Conditional Moment Closure combustion model with RANS and LES," *SAE Int. J. Engines **9** (4) in press, 2016.*
- L. Zeugin, C.K. Blomberg, M. Bolla, K. Boulouchos and Y.M. Wright: "Numerical simulations of ECN 'Spray A' split injection using LES-CMC", accepted for presentation at the LES4ICE, 29/30. Nov. 2016, IFPEN, Rueil-Malmaison, Paris, France.

8.2 The following publications are currently in preparation:

- C. Blomberg, Y. M. Wright and K. Boulouchos, "A Phenomenological HCCI Combustion Model in 0D and 3D-CFD," *in preparation for FUEL*.

9 Co-funding

This project was co-funded by the **Swiss Oil Association** (grant no. 3'34'12) and the **Research Association for Combustion Engines eV** (Forschungsvereinigung Verbrennungskraftmaschinen e.V. Project "fuel indices II./ Kraftstoffkennzahlen II.").

10 References

[1] Reitz RD. Directions in internal combustion engine research. Combust Flame 2013;160:1–8. doi:10.1016/j.combustflame.2012.11.002.

[2] Yang Y, Dec JE, Dronniou N, Sjöberg M. Tailoring HCCI heat-release rates with partial fuel stratification: Comparison of two-stage and single-stage-ignition fuels. Proc Combust Inst 2011;33:3047–55. doi:10.1016/j.proci.2010.06.114.

[3] Sjöberg M, Dec JE. Comparing late-cycle autoignition stability for single- and two-stage ignition fuels in HCCI engines. Proc Combust Inst 2007;31:2895–902. doi:10.1016/j.proci.2006.08.010.

[4] Musculus MPB, Miles PC, Pickett LM. Conceptual models for partially premixed low-temperature diesel combustion. Prog Energy Combust Sci 2013;39:246–83. doi:10.1016/j.pecs.2012.09.001.

[5] Hartmann M, Starke R. Kraftstoffkennzahlen – TP 1 Stoßwellenrohr, Untersuchungen der Zündverzugszeiten im Stoßwellenrohr. FVV Manag Rep 2010.

[6] Boulouchos K, Vandersickel A, Heinl E, Teetz C. Kraftstoffkennzahlen – TP 2 Reaktionskinetik - Entwicklung phänomenologischer Reaktionsmodelle für eine homogene selbstgezündete Verbrennung (HCCI). FVV Manag Rep 2011.

[7] Boulouchos K, Mitakos DA, Schneider B, Heinl E, Teetz C. Kraftstoffkennzahlen – TP 3 Einhubtriebwerk (EHT) - Untersuchung des Homogenen-Zündverhalten im Einhubtriebwerk. FVV Manag Rep 2011.

[8] Bargende M, Beck S, Heinl E, Teetz C. Kraftstoffkennzahlen – TP 5 Einzylindermotor PKW - Experimentelle Untersuchungen an einem PKW-Einzylindermotor zur Identifikation des Kraftstoffeinflusses auf eine homogenisierte selbstgezündete Verbrennung (HCCI). FVV Manag Rep 2011.

[9] Pischinger S, Rajamini V, Heinl E, Teetz C. Kraftstoffkennzahlen – TP 6 - Nfz-Einzylindermotor. FVV Manag Rep 2011.

[10] Weisser GA. Modelling of Combustion and Nitric Oxide Formation for Medium-Speed DI Diesel Engines: A comparative Evaluation of Zero- and Three-Dimensional Approaches. ETH Zurich PhD Thesis 2001. doi:10.3929/ethz-a-004317089.

[11] Vandersickel A. Two Approaches to Auto-ignition Modelling for HCCI Applications. ETH Zurich PhD Thesis 2011. doi:10.3929/ethz-a-006776450.

[12] Livengood JC, Wu PC. Correlation of autoignition phenomena in internal combustion engines and rapid compression machines. Symp Combust 1955;5:347–56. doi:10.1016/S0082-0784(55)80047-1.

[13] Mitakos DA, Blomberg C, Wright YM, Obrecht P, Schneider B, Boulouchos K. Integration of a Cool-Flame Heat Release Rate Model into a 3-Stage Ignition Model for HCCI Applications and Different Fuels. SAE Tech Pap 2014. doi:10.4271/2014-01-1268.

[14] Blomberg C, Mitakos D, Bardi M, Boulouchos K, Wright YM, Vandersickel A. Extension of the Phenomenological 3-Arrhenius Auto-Ignition Model for Six Surrogate Automotive Fuels. SAE Int J Engines 2016;3. doi:10.4271/2016-01-0755.

[15] Skeen S, Manin J, Pickett LM. Visualization of Ignition Processes in High-Pressure Sprays with Multiple Injections of n-Dodecane. SAE Int J Engines 2015;8:696–715. doi:10.4271/2015-01-0799.

[16] Skeen SA, Manin J, Pickett LM, Cenker E, Bruneaux G, Kondo K, et al. A Progress Review on Soot Experiments and Modeling in the Engine Combustion Network (ECN). SAE Int J Engines 2016;9. doi:10.4271/2016-01-0734.

[17] Yao T, Pei Y, Zhong B-J, Som S, Lu T. A hybrid mechanism for n-dodecane combustion with optimized low-temperature chemistry. 9th U.S. Natl. Combust. Meet., Cincinnati: 2015.

[18] Schmitt M, Frouzakis CE, Tomboulides AG, Wright YM, Boulouchos K. Direct numerical simulation of the effect of compression on the flow, temperature and composition under engine-like conditions. Proc Combust Inst 2014. doi:10.1016/j.proci.2014.06.097.

[19] Weisser G, Tanner FX, Boulouchos K. Modeling of Ignition and Early Flame Development with Respect to Large Diesel Engine Simulation. SAE Tech Pap 1998. doi:10.4271/981451.

[20] Vandersickel A, Hartmann M, Vogel K, Wright YM, Fikri M, Starke R, et al. The autoignition of practical fuels at HCCI conditions: High-pressure shock tube experiments and phenomenological modeling. Fuel 2011;93:492–501. doi:10.1016/j.fuel.2011.10.062.

[21] Bardi M, Blomberg C, Mitakos DA, Schneider B, Wright YM, Boulouchos K. Effect of fuel composition and in cylinder conditions on HCCI combustion in an optically accessible Rapid Compression Expansion Machine. Prog n.d.

[22] Sung C-J, Curran HJ. Using rapid compression machines for chemical kinetics studies. Prog Energy Combust Sci 2014;44:1–18. doi:10.1016/j.pecs.2014.04.001.

[23] Mitakos DA. Experimental Investigations for Phenomenological Modelling of Two-Stage Auto-Ignition under HCCI Conditions. ETH Zurich PhD Thesis 2014. doi:10.3929/ethz-a-010421729.

[24] Obrecht P. WEG - Verbrennungsanalyse: Berechnung des Wärmeentwicklungsgesetzes. Version 15 2008.

[25] Burcat A, Branko R. Third millennium ideal gas and condensed phase thermochemical database for combustion with updates from active thermochemical tables. Tech Rep 2005;ANL-05/20:ANL – 05/20 TAE 960.

[26] CD-adapco. STAR-CD Methodology. Version 420 2013.

[27] Tsurushima T. A new skeletal PRF kinetic model for HCCI combustion. Proc Combust Inst 2009;32:2835–41. doi:10.1016/j.proci.2008.06.018.

[28] Saxena S, Bedoya ID. Fundamental phenomena affecting low temperature combustion and HCCI engines, high load limits and strategies for extending these limits. Prog Energy Combust Sci 2013;39:457–88. doi:10.1016/j.pecs.2013.05.002.

[29] Singh S, Reitz RD, Musculus MPB, Lachaux T. Validation of engine combustion models against detailed in-cylinder optical diagnostics data for a heavy-duty compression-ignition engine. Int J Engine Res 2007;8 :97–126. doi:10.1243/14680874JER02406.

[30] Brakora J, Reitz R. A Comprehensive Combustion Model for Biodiesel-Fueled Engine Simulations. SAE Tech Pap 2013. doi:10.4271/2013-01-1099.

[31] Pei Y, Som S, Pomraning E, Senecal PK, Skeen SA, Manin J, et al. Large eddy simulation of a reacting spray flame with multiple realizations under compression ignition engine conditions. Combust Flame 2015. doi:10.1016/j.combustflame.2015.08.010.

[32] Wright Y, De Paola G, Boulouchos K, Mastorakos E. Simulations of spray autoignition and flame establishment with two-dimensional CMC. Combust Flame 2005;143:402–19. doi:10.1016/j.combustflame.2005.08.022.

[33] Wright YM. Numerical investigation of turbulent spray combustion with conditional moment closure. ETH Zurich PhD Thesis 2006. doi:10.3929/ethz-a-005228336.

[34] Wright YM, De Paola G, Boulouchos K, Mastorakos E. Simulations of spray autoignition and flame establishment with two-dimensional CMC. Combust Flame 2005;143:402–19.

[35] Wright YM, Margari O-N, Boulouchos K, De Paola G, Mastorakos E. Experiments and Simulations of n-Heptane Spray Auto-Ignition in a Closed Combustion Chamber at Diesel Engine Conditions. Flow, Turbul Combust 2010;84:49–78. doi:10.1007/s10494-009-9224-0.

[36] Farrace D, Bolla M, Wright YM, Boulouchos K. Predicting In-Cylinder Soot in a Heavy-Duty Diesel Engine for Variations in SOI and TDC Temperature Using the Conditional Moment Closure Model. SAE Int J Engines 2013;6:1580–93. doi:10.4271/2013-24-0016.

[37] Bolla M, Wright YM, Boulouchos K, Borghesi G, Mastorakos E. Soot formation modelling of n-heptane sprays under diesel engine conitions using the Conditional Moment Closure approach. Combust Sci Technol 2013;185:766–93. doi:10.1080/00102202.2012.752362.

[38] Bolla M, Farrace D, Wright YM, Boulouchos K, Mastorakos E. Influence of turbulence–chemistry interaction for n -heptane spray combustion under diesel engine conditions with emphasis on soot

formation and oxidation. Combust Theory Model 2014;18:330–60. doi:10.1080/13647830.2014.898795.

[39] Bolla M, Wright YM, Boulouchos K. Application of a Conditional Moment Closure Combustion model to a large two-stroke marine Diesel engine reference experiment. 8th Int. Conf. Model. Diagnostics Adv. Engine Syst., Fukuoka, Japan: 2012.

[40] De Paola G, Mastorakos E, Wright YM, Boulouchos K. Diesel engine simulations with multi-dimensional conditional moment closure. Combust Sci Technol 2008;180:883–99. doi:Doi 10.1080/00102200801894273.

[41] Wright YM, Boulouchos K, De Paola G, Mastorakos E. Multi-dimensional Conditional Moment Closure Modelling Applied to a Heavy-duty Common-rail Diesel Engine. SAE Int J Engines 2009;2:714–26. doi:10.4271/2009-01-0717.

[42] Bolla M, Farrace D, Wright YM, Boulouchos K. Modelling of soot formation in a heavy-duty diesel engine with conditional moment closure. Fuel 2014;117:309–25. doi:DOI 10.1016/j.fuel.2013.09.041.

[43] Farrace D, Bolla M, Wright YM, Boulouchos K. Numerical study of the influence of EGR on in-cylinder soot characteristics in a heavy-duty diesel engine using CMC. SAE Int J Engines 2014;7:256–68. doi:http://dx.doi.org/10.4271/2014-01-1134.

[44] Pandurangi S, Wright YM, Brückner C, Kyrtatos P, Boul. Impact of pilot injections on ignition behaviour at low in-cylinder temperatures from extreme miller valve timing in a heavy-Duty Diesel engine. Proc. 15th Int. Conf. Numer. Combust. Avignon, Fr., Avignon, France: 2015.

[45] Pandurangi SS, Frapolli N, Bolla M, Boulouchos K, Wright YM. Influence of EGR on Post-Injection Effectiveness in a Heavy-Duty Diesel Engine Fuelled with n-Heptane. SAE Int J Engines 2014;7:1851–62. doi:10.4271/2014-01-2633.

[46] Frapolli NN, Bolla M, Boulouchos K, Wright YM, Boulouchos K, Wright YM. Simulations of In-Cylinder Processes in a Diesel Engine Operated with Post-Injections Using an Extended CMC Model. SAE Tech Pap 2014. doi:10.4271/2014-01-2571.

[47] Barro C, Pandurangi S, Meyer P, Boulouchos K, Elbert P, Wright YM. THE Post Injection: Coalescence of 3D CFD-CMC Simulation, 2D Visualizations in a Constant Volume Chamber and Application in a Modern Passenger Car Diesel Engine. SAE Tech Pap 2015. doi:10.4271/2015-24-2515.

[48] Wright YM, Borghesi G, Mastorakos E, Boulouchos K. Predicting the stochastic behaviour of autoignition in Diesel-like environments with LES-CMC. Int Conf LES Intern Combust Engine Flows 2012 (LES4ICE), Rueil-Malmaison, Fr 2012

[49] Farrace D, Wright YM, Boulouchos K. Assessment of LES-CMC Simulations for Spray A Combustion. Int Conf LES Intern Combust Engine Flows 2014 (LES4ICE), Rueil-Malmaison, Fr 2014

[50] Bolla M, Farrace D, Wright YM, Boulouchos K. Modelling of soot formation in a heavy-duty diesel engine with conditional moment closure. Fuel 2014;117:309–25. doi:10.1016/j.fuel.2013.09.041.

[51] Zeugin L. Qualitative Study of Mulitple Injections in 3D-CFD. ETH Zurich Semester Thesis, Aerothermochemistry Combust Syst Lab 2015.

[52] Bolla M. Modeling soot formation in diesel engines using conditional moment closure. ETH Zurich PhD Thesis 2013. doi:10.3929/ethz-a-010087266.

[53] Farrace D, Sakellarakis D, Bolla M, Wright YM, Boulouchos K. Numerical Analysis of Soot Dynamics for Spray A. Prep Flow, Turbul Combust 2016.

[54] Farrace D, Panier R, Schmitt M, Boulouchos K, Wright YM. Analysis of Averaging Methods for Large Eddy Simulations of Diesel Sprays. SAE Int J Fuels Lubr 2015;8:568–80. doi:10.4271/2015-24-2464.

[55] Bottone F, Kronenburg A, Gosman D, Marquis A. The Numerical Simulation of Diesel Spray Combustion with LES-CMC. Flow, Turbul Combust 2012;89:651–73. doi:10.1007/s10494-012-9415-y.

[56] Navarro-Martinez S, Kronenburg A. LES–CMC simulations of a lifted methane flame. Proc Combust Inst 2009;32:1509–16. doi:10.1016/j.proci.2008.06.178.

[57] Garmory A, Mastorakos E. Sensitivity analysis of LES–CMC predictions of piloted jet flames. Int J Heat Fluid Flow 2013;39:53–63. doi:10.1016/j.ijheatfluidflow.2012.11.007.

[58] Navarro-Martinez S, Kronenburg A. Flame Stabilization Mechanisms in Lifted Flames. Flow, Turbul Combust 2011;87:377–406. doi:10.1007/s10494-010-9320-1.

[59] Triantafyllidis A, Mastorakos E, Eggels RLGM. Large Eddy Simulations of forced ignition of a non-premixed bluff-body methane flame with Conditional Moment Closure. Combust Flame 2009;156:2328–45. doi:10.1016/j.combustflame.2009.05.005.

[60] Garmory A, Mastorakos E. Numerical simulation of oxy-fuel jet flames using unstructured LES–CMC. Proc Combust Inst 2015;35:1207–14. doi:10.1016/j.proci.2014.05.032.

[61] Knox BW, Genzale CL, Pickett LM, Garcia-Oliver JM, Vera-Tudela W. Combustion Recession after End of Injection in Diesel Sprays. SAE Int J Engines 2015;8:679–95. doi:10.4271/2015-01-0797.

[62] Yao M, Zheng Z, Liu H. Progress and recent trends in homogeneous charge compression ignition (HCCI) engines. Prog Energy Combust Sci 2009;35:398–437. doi:10.1016/j.pecs.2009.05.001.